


5-2014

Atomic-Scale Characterization and Manipulation of Freestanding Graphene Using Adapted Capabilities of a Scanning Tunneling Microscope

Steven Barber

University of Arkansas, Fayetteville

Follow this and additional works at: <http://scholarworks.uark.edu/etd>

 Part of the [Condensed Matter Physics Commons](#), and the [Optics Commons](#)

Recommended Citation

Barber, Steven, "Atomic-Scale Characterization and Manipulation of Freestanding Graphene Using Adapted Capabilities of a Scanning Tunneling Microscope" (2014). *Theses and Dissertations*. 2363.
<http://scholarworks.uark.edu/etd/2363>

This Dissertation is brought to you for free and open access by ScholarWorks@UARK. It has been accepted for inclusion in Theses and Dissertations by an authorized administrator of ScholarWorks@UARK. For more information, please contact scholar@uark.edu, ccmiddle@uark.edu.

Atomic-Scale Characterization and Manipulation of Freestanding Graphene
Using Adapted Capabilities of a Scanning Tunneling Microscope

Atomic-Scale Characterization and Manipulation of Freestanding Graphene
Using Adapted Capabilities of a Scanning Tunneling Microscope

A dissertation submitted in partial fulfillment
of the requirements for the degree of
Doctor of Philosophy in Physics

by

Steven Barber
Harding University
Bachelor of Science in Physics, 2009
University of Arkansas
Master of Science in Physics, 2012

May 2014
University of Arkansas

This dissertation is approved for recommendation to the Graduate Council.

Dr. Paul Thibado
Dissertation Director

Dr. Julio Gea-Banacloche
Committee Member

Dr. Surendra Singh
Committee Member

Dr. Huaxiang Fu
Committee Member

Dr. Hameed Naseem
Committee Member

ABSTRACT

Graphene was the first two-dimensional material ever discovered, and it exhibits many unusual phenomena important to both pure and applied physics. To ensure the purest electronic structure, or to study graphene's elastic properties, it is often suspended over holes or trenches in a substrate. The aim of the research presented in this dissertation was to develop methods for characterizing and manipulating freestanding graphene on the atomic scale using a scanning tunneling microscope (STM). Conventional microscopy and spectroscopy techniques must be carefully reconsidered to account for movement of the extremely flexible sample.

First, the acquisition of atomic-scale images of freestanding graphene using the STM and the ability to pull the graphene perpendicular to its plane by applying an electrostatic force with the STM tip are demonstrated. The atomic-scale images contained surprisingly large corrugations due to the electrostatic attractive force varying in registry with the local density of states. Meanwhile, a large range of control over the graphene height at a point was obtained by varying the tip bias voltage, and the application to strain engineering of graphene's so-called pseudomagnetic field is examined. Next, the effect of the tunneling current was investigated. With increasing current, the graphene sample moves away from the tip rather than toward it. It was determined that this must be due to local heating by the electric current, causing the graphene to contract because it has a negative coefficient of thermal expansion.

Finally, by imaging a very small area, the STM can monitor the height of one location over long time intervals. Results sometimes exhibit periodic behavior, with a frequency and amplitude that depend on the tunneling current. These fluctuations are interpreted as low-frequency flexural phonon modes within elasticity theory. All of these findings set the foundation for employing a STM in the study of freestanding graphene.

ACKNOWLEDGEMENTS

I would like to first thank my research advisor Dr. Paul Thibado for his guidance and encouragement over the last few years. I feel very fortunate to have been part of his group, and I share the credit for our success with him, Dr. Peng Xu, and my fellow hard-working students Dejun Qi, Matt Ackerman, Kevin Schoelz, Gobind Basnet, Cameron Cook, and Josh Thompson. We have also been supported by a number of invaluable collaborators on various projects. My special thanks to Drs. Salvador Barraza-Lopez, Yurong Yang, and Laurent Bellaiche at the University of Arkansas, Dr. Lifeng Dong at Missouri State University, and Drs. Mehdi Neek-Amal and Francois Peeters at the University of Antwerp.

I have had an excellent dissertation committee whom I appreciate greatly for taking the time to review my progress and results. In addition to Dr. Thibado, I thank Drs. Julio Gea-Banacloche, Surendra Singh, and Huaxiang Fu from the Department of Physics and Dr. Hameed Naseem from the Department of Electrical Engineering. Moreover, all my teachers have my gratitude for investing their time to instill the love of learning in me.

I furthermore gratefully acknowledge the financial aid provided by several sources. Grants from the National Science Foundation and the Office of Naval Research have helped fund our operating costs and my two-year research assistantship. The University of Arkansas Graduate School generously awarded me a four-year Doctoral Academy Fellowship in addition to the teaching assistantship offered by the physics department. I especially express thanks to Mrs. Jane Hughes for sponsoring the Raymond H. Hughes Graduate Fellowship, which I received in my last semester of study.

Finally, I could not have made it to this point without my parents, who always believed in me, and my loving wife, for whom I thank God every day. This is for you and because of you.

TABLE OF CONTENTS

I. INTRODUCTION.....	1
A. PROPERTIES OF GRAPHENE.....	1
B. FREESTANDING GRAPHENE	2
C. SYNOPSIS	3
II. STM THEORY AND OPERATION	5
A. OPERATIONAL PRINCIPLES.....	5
B. SYSTEM DESCRIPTION	6
C. ELECTROCHEMICAL TIP ETCHING.....	9
III. STM IMAGING AND MANIPULATION OF FREESTANDING GRAPHENE.....	10
A. SAMPLE DESCRIPTION AND PREPARATION	10
B. IMAGING WITH ENHANCED ATOMIC CORRUGATIONS.....	12
Experiment and Results.....	12
Discussion	14
C. CONSTANT-CURRENT ELECTROSTATIC MANIPULATION	16
Experiment and Results.....	16
Discussion	17
D. IMAGE-CHARGE MODEL OF ELECTROSTATIC ATTRACTION	20
Setup and Derivation.....	20
Calculation of Force as a Function of Voltage.....	24
E. LARGE PSEUDOMAGNETIC FIELDS	27
Shape of the Graphene Membrane	27
Calculation of the Strain-Induced Field	29

F.	EFFECTS OF TUNNELING CURRENT ON GRAPHENE HEIGHT	31
	Experimental Results and Discussion	31
	Modeling Thermal Contraction of Graphene	35
IV.	MEASURING LOW-FREQUENCY HEIGHT FLUCTUATIONS.....	40
A.	DEMONSTRATION OF EXPERIMENTAL TECHNIQUE.....	40
B.	PERIODIC FLUCTUATIONS	43
	Data and Analysis.....	43
	Agreement with Elasticity Theory	46
C.	MIRROR BUCKLING.....	49
V.	SUMMARY	53
	References	55
	Appendix A: Bessel Function Ratio	64
	Appendix B: Graphene Height under Central Load	66
	Appendix C: Pseudomagnetic Field Calculation.....	68
	Appendix D: The Rubber Band Problem	70
	Appendix E: Graphene Height as Function of Current	72
	Appendix F: Autocovariance and Periodogram Definitions	74
	Appendix G: Savitzky-Golay Program	76
	Appendix H: Periodogram Code	105

LIST OF FIGURES

<i>Fig. 1:</i> Orientation of Tip and Sample	8
<i>Fig. 2:</i> SEM Images of Freestanding Graphene.....	11
<i>Fig. 3:</i> Atomic-Scale STM Images of Graphene	13
<i>Fig. 4:</i> Schematics of Freestanding Graphene Attracted to a STM Tip.....	15
<i>Fig. 5:</i> Graphene Height as a Function of Voltage at Constant Current.....	18
<i>Fig. 6:</i> Sphere-Plane Model of Electrostatic Attraction.....	21
<i>Fig. 7:</i> Analysis of $F \propto V^2$	23
<i>Fig. 8:</i> Possible Force Curves as a Function of Voltage.....	25
<i>Fig. 9:</i> Calculated Graphene Shape under Central Point Load.....	30
<i>Fig. 10:</i> Graphene Height as a Function of Current at Constant Voltage.....	32
<i>Fig. 11:</i> Adjusted $Z(V)$ and $F(Z)$ Curves.....	34
<i>Fig. 12:</i> Illustration of the Entropic Rubber Band Model.....	36
<i>Fig. 13:</i> Comparizon of $Z(I)$ Data to Mathematical Model.....	38
<i>Fig. 14:</i> Example of Random Thermal Fluctuations.....	41
<i>Fig. 15:</i> Fluctuations Exhibiting Periodic Components.....	44
<i>Fig. 16:</i> Dependence of Frequency and Amplitude on Current.....	48
<i>Fig. 17:</i> Fluctuations with a Sudden Large Jump in Height	50
<i>Fig. 18:</i> Diagram of Mirror Buckling	52

LIST OF ABBREVIATIONS

Standard abbreviations are used for all units of measurement.

Accepted chemical symbols are used for all elements and compounds.

2D.....two-dimensional

CVD chemical vapor deposition

DOS.....density of states

LDOS local density of states

SEM scanning electron microscopy (or microscope)

STM scanning tunneling microscopy (or microscope)

STS..... scanning tunneling spectroscopy

TEM transmission electron microscopy (or microscope)

UHV ultra-high vacuum

UPS uninterruptable power supply

LIST OF SYMBOLS

The following letters are used to represent corresponding constants and variables.

ϵ_0 permittivity of free space

\hbar the reduced Planck constant

a radius of a sphere representing the STM tip apex

e the elementary electric charge

F electrostatic attractive force between the STM tip and sample

I measured STM tunneling current

I_0 tunneling current setpoint the STM seeks to maintain by adjusting the tip height

m mass of an electron

s distance between the STM tip apex and the sample surface

T temperature of graphene under the STM tip

V voltage applied to the STM tip relative to a grounded sample

V_0 constant voltage applied to the STM tip while other parameters change

Z measured height of the STM tip

I. INTRODUCTION

The most important and surprising discovery of condensed matter physics in the last decade was the isolation of graphene [1], for which Andre Geim and Konstantin Novoselov were awarded the 2010 Nobel Prize in Physics. Graphene can be described as a single atomic layer of the common semimetal graphite, or as an unrolled single-wall carbon nanotube. As such, it is a two-dimensional (2D) material composed entirely of carbon, with the sp^2 -bonded atoms forming a honeycomb lattice that contains two atoms per unit cell. Prior to the confirmation of the existence of isolated graphene, long-range 2D crystalline order was widely considered impossible [2], a result of well-established theory [3] and numerous experiments in which thin films rolled up or decomposed below a certain minimum thickness [4-6]. Graphene prompted a reconsideration of that long-standing supposition and opened the door to a flood of other 2D crystals. However, this distinction is only the beginning of what makes graphene so special.

A. PROPERTIES OF GRAPHENE

The band structure of graphene was first calculated in 1946 as the starting point for studying graphite [7]. Much of the theory surrounding graphene was thus able to develop long before experiments were possible or even imagined. The most fascinating prediction is that the low-energy charge carriers in graphene mimic massless Dirac fermions, meaning they exhibit a linear electronic dispersion but travel at the Fermi velocity ($\approx 1 \times 10^6$ m/s) instead of the speed of light [8]. This leads to the manifestation of several remarkable phenomena typically reserved for quantum electrodynamics. For example, the cyclotron mass in graphene depends on the square root of the electronic density, rather than remaining constant [9]. It is also possible to test the Klein tunneling paradox [10], observe a half-integer quantum Hall effect [11], and achieve micrometer-scale ballistic transport [12].

In addition to curious and useful electronic properties, graphene also possesses noteworthy mechanical and structural characteristics. Most famously, despite being only one atom thick, it has been called the “strongest material ever measured” [13]. This rigidity can be attributed to the stiff nature of the in-plane sigma bonds, yet perpendicular to the plane it remains very flexible. Furthermore, graphene is impermeable to gases [14] and suitable for high-frequency mechanical actuation by electrical or optical means [15]. Interestingly, contrary to the common theoretical description and 2D designation, freestanding graphene is not perfectly flat, but rather displays intrinsic ripples around 5 nm wide and 0.5 nm high [16-18]. Most researchers believe these are the key to understanding graphene’s unexpected stability, but the exact mechanism responsible is still under debate [19]. All these intriguing properties discussed so far shed some light on the intense excitement and research activity that has been associated with graphene since its discovery.

B. FREESTANDING GRAPHENE

There are many methods of producing and handling graphene. The first samples were fabricated by micromechanical cleavage of graphite, which results in especially pristine flakes for sensitive experiments [20, 21]. However, the flakes are typically miniscule, only a small fraction of them are monolayer, and they must be viewed on an oxidized silicon wafer under an optical microscope to be identified [22]. Much work has also been devoted to reliably forming high-quality epitaxial graphene by thermal decomposition of SiC wafers [23, 24]. This has the advantage of being the most direct path to graphene-based electronics, but the disadvantages of expense and difficulty in controlling uniform growth [25, 26]. The final common method of graphene production is chemical vapor deposition (CVD) on certain metallic surfaces [27-29]. Copper is probably the most popular choice because it naturally limits the growth to one layer

that is continuous across various topographical features and can be transferred to other surfaces on a large scale [30-32]. Unfortunately, no matter the method of production or transfer, graphene on a substrate maintains some level of interaction with the substrate, which degrades the intrinsic mobility [33, 34] through local effects, such as charged-impurity scattering [35], and nonlocal phenomena, such as remote phonon scattering [36]. In order to study pure graphene, it becomes necessary to suspend the sections to be tested.

This has been accomplished in numerous ways, but almost always with impressive results. For example, the record-breaking carrier mobility in graphene was only measured after partially etching away the SiO₂ under a mechanically exfoliated flake [37, 38]. Similarly, pristine cleaved layers have been placed over prefabricated trenches in a Si/SiO₂ substrate to measure graphene's negative thermal expansion coefficient [39] and superb thermal conductivity [40]. Freestanding graphene, transferred onto a gold or copper scaffold, is also convenient for transmission electron microscopy (TEM), with the best images achieving atomic resolution [41]. Moreover, suspension is the only way for atomic force microscopy to determine the effective spring constant, Young's modulus, and other elastic parameters of graphene [42, 43]. Clearly, a thorough examination of freestanding graphene is a necessary and valuable step toward realizing the full potential of this remarkable material. Applications are envisioned in almost every field, including high-performance flexible electronics, superior solar cells and fuel cells, ultrasensitive measurement devices, and advanced *in vivo* drug delivery [44, 45].

C. SYNOPSIS

In this dissertation, I will explore ways to characterize and manipulate freestanding graphene using a scanning tunneling microscope (STM). Focus will be given to proper interpretation of the data, in light of significant interactions between the STM tip and graphene,

in order to deduce atomic-scale properties of the sample. I will begin with an overview of STM and a description of the system and sample used, then discuss the challenges and peculiarities of imaging freestanding graphene. Next, attention will turn to constant-current scanning tunneling spectroscopy (STS) as a method for pulling on the membrane and introducing strain, with approaches for calculating the applied electrostatic force and induced pseudomagnetic field. Complementing that strategy, I also consider constant-voltage STS, which reveals the unexpected influence of the tunneling current. Finally, a new procedure is introduced for recording height fluctuations of a single atom in the graphene sheet, and low-frequency periodic oscillations are observed and analyzed. Taken together, these capabilities form a useful set of STM experiments that will provide a fundamental understanding of freestanding graphene, its functionalized derivatives, and any similar 2D materials of interest.

II. STM THEORY AND OPERATION

Invention of the STM is credited to Gerd Binnig and Heinrich Rohrer, who won the 1986 Nobel Prize in Physics for their work [46]. They experimentally demonstrated quantum tunneling in vacuum by measuring an electrical resistance that depended exponentially on the width of the gap between a tungsten tip and platinum sample [47]. Then they cleverly applied this ability to acquire the first atomic-resolution image of the Si(111) 7×7 surface [48]. Atomic-resolution microscopy was a breakthrough that revolutionized surface physics by revealing never-before-seen details in real space [49-51]. Furthermore, the precision of the newly developed instrumentation allowed positioning of the probe with atomic accuracy for sensitive, local spectroscopic experiments [52]. If microscopy and spectroscopy were not enough, the STM was also shown to be capable of manipulating single atoms adsorbed on a surface, adding yet another dimension to its impressive capabilities [53-55]. In this chapter, I will summarize the basics of STM as they pertain to the rest of this dissertation and describe the system used in my experiments. For a more complete review of STM, consult Ref. [56].

A. OPERATIONAL PRINCIPLES

In STM an atomically sharp metal tip is brought within a few angstroms of a conducting sample surface, typically in vacuum. When a potential difference is applied between the two, some electrons will be able to undergo quantum mechanical tunneling through the vacuum, the direction of current depending on the applied bias voltage. The tunneling current (I) decreases exponentially as the tip-sample separation (s) increases, according to:

$$I \propto e^{-s\sqrt{8m\phi}/\hbar}, \quad (1)$$

where m is the electron mass, ϕ is the effective local potential barrier height, and \hbar is the reduced Planck constant [57, 58]. This means that small changes in the gap result in large

changes in the current, making it possible to achieve excellent vertical resolution (~ 0.01 nm). Likewise, with an adequately sharp tip, almost all the measured current will be following the shortest possible path, from the tip apex to the region of the surface directly below the apex. Thus quantum tunneling also facilitates superb lateral resolution (~ 0.1 nm). When the tip is raster scanned over a surface, with the tip height controlled via a feedback loop programmed to keep the tunneling current constant, a topographical map is formed which traces a constant local density of states (LDOS). This is the basis of constant-current microscopy. The necessary precision of movement is achieved using piezoelectric actuators.

The STM can also be used to perform spectroscopy, especially to map the sample's density of states (DOS). With the tip stationary at one lateral location and a constant height determined by an initial "setpoint" current and voltage, the potential bias (V) is ramped and the tunneling current is recorded. If one plots $(dI/dV)/(I/V) = (d \ln I)/(d \ln V)$ versus V , the peaks in the graph correspond to peaks in the DOS [59, 60]. Another option for spectroscopy is "feedback-on" spectroscopy, in which the tip height is allowed to change in order to maintain the setpoint current. In this case, one may ramp either the voltage or setpoint current and measure the change in tip height. At constant V , for example, an apparent local barrier height (ϕ_A) can be calculated by this method according to [61]:

$$\phi_A[\text{eV}] = \frac{\hbar^2}{8m} \left(\frac{d \ln I}{ds} \right)^2. \quad (2)$$

Feedback-on spectroscopy is less common but will be critical to the experiments performed for this dissertation.

B. SYSTEM DESCRIPTION

The STM used in the following experiments is an Omicron low-temperature model. Though operated at room temperature for our research, this model is somewhat unusual in that

the tip points upward at a downward-facing sample surface, as depicted in Fig. 1. (Note that later diagrams may not reflect this orientation.) It is important to understand, however, that in graphs showing the tip height (Z), an increase in Z corresponds to moving away from the sample, even though this is downward motion relative to the Earth. This convention is indicated in Fig. 1 by the plus sign next to the arrow. Another notable convention is that our samples are electrically grounded for all experiments. Therefore, the system voltage reported (V) is always the bias applied to the tip, measured relative to ground and the sample.

This STM operates under ultra-high vacuum (UHV) conditions, meaning the mean free path for molecules in the chamber is on the order of 100 km. Its base pressure is about 10^{-10} mbar, and the pressure during experiments was typically around 10^{-9} mbar. UHV is achieved and maintained through a combination of techniques and devices, including baking the system at high temperature, all-metal seals, a turbopump, an ion pump, and a titanium sublimation pump. Macroscopic positioning of the STM tip is accomplished using stick-slip piezoelectric actuators, and microscopic positioning relies on a piezoelectric single-tube scanner. Furthermore, the STM has been customized to operate two orthogonal tips simultaneously [62].

It is critical that the STM be free of both mechanical and electrical noise. It comes equipped with a spring suspension system with a resonance frequency of about 2 Hz and an eddy-current damping mechanism to remove vibrations from the STM stage. In addition, the entire UHV chamber is supported by an active vibration-cancellation table, which was only recently added. To minimize electrical noise, the STM and all its supporting electronics are powered by a large uninterruptible power supply (UPS). The batteries of the UPS provide a quiet electrical source and prevent equipment damage or loss of data due to power failures. In

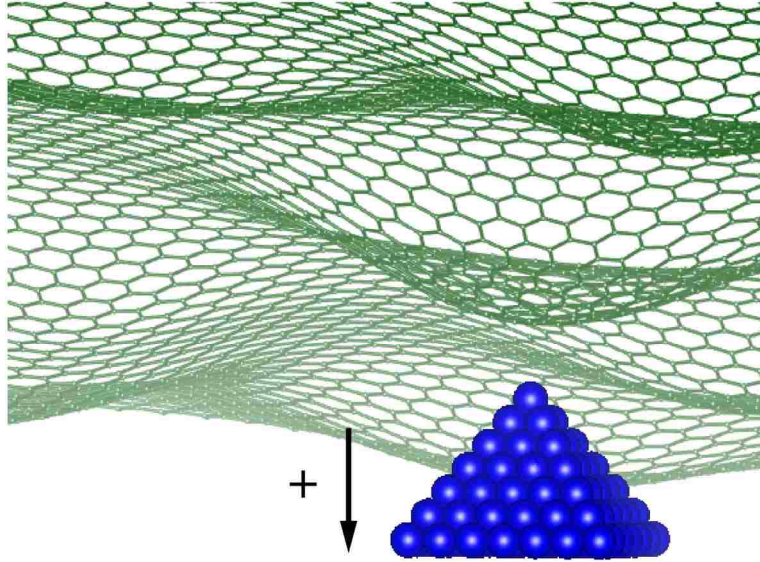


Figure 1: Depiction of a biased STM tip as it is brought near a suspended, grounded graphene sample with intrinsic roughening. As in our STM system, the tip approaches from below, but the measured tip height increases as it moves away from the sample.

addition, a private grounding rod was installed outside the lab for the STM to have a clean electrical ground.

C. ELECTROCHEMICAL TIP ETCHING

Atomically sharp, mechanically stable tips are critical for most STM experiments. Therefore, we have devoted significant effort to developing an easy and reliable etching method. STM tips are manufactured in-house from 0.25-mm-diameter, polycrystalline tungsten wire, which is electrochemically etched in a sodium hydroxide solution using a custom double-lamella setup with an automatic gravity-switch cutoff [63]. Compared to other methods tested, this one was the most likely to produce a tip both sharp and stable enough to achieve atomic-resolution images on highly oriented pyrolytic graphite. It combines precision, ease of operation, and a fast cutoff time. The design was later improved further by applying an etch stop to limit the length of wire exposed to the etchant, while still permitting the use of a thick, stable lamella [64]. After etching, the tips are gently rinsed with distilled water, briefly dipped in a concentrated hydrofluoric acid solution to remove surface oxides [65], and promptly transferred through a load-lock into the STM chamber where they can be temporarily stored or immediately utilized.

III. STM IMAGING AND MANIPULATION OF FREESTANDING GRAPHENE

A. SAMPLE DESCRIPTION AND PREPARATION

All graphene samples were grown via CVD by a commercial provider.* The freestanding graphene was first grown on nickel foil, which was then placed graphene-down over ultrafine, 2000-mesh copper TEM grids. The circular TEM grids are 3.05 mm in diameter and feature a scaffold of square holes 7.5 μm wide and bar supports 5 μm wide. When the nickel is chemically etched away, graphene is left behind, partially supported by the copper bars and partially suspended over the square holes. The transferred graphene is reported to be from one to six monolayers thick with 60% to 90% coverage. The high coverage was confirmed by scanning electron microscopy (SEM), and example images are shown in Fig. 2. In addition, energy dispersive X-ray analysis confirmed that the surface was free of detectable contamination. For a non-flexible control sample, single-layer graphene grown on polycrystalline copper foil was used without transferring it to a different substrate.

Prior to loading into the STM chamber, all samples were mounted on standard flat tantalum plates using silver paint. The grids can be mounted with the graphene side up or down, and both options were sometimes employed. When facing down, the grid was elevated by a stand-off support so that the graphene could not come into contact with the sample holder. The STM tip can still access the freestanding graphene through the holes of the copper grid, and we had fewer problems with stability in this configuration. Once the sample was loaded into the STM chamber, only lamp-type heating was applied, and no other heating or annealing was done to the sample. Excessive annealing of the freestanding graphene may cause macroscopic texturing due to the grid expanding and the graphene contracting during the heating process [39].

*Graphene Supermarket, Calverton, NY (<http://www.graphene-supermarket.com>).

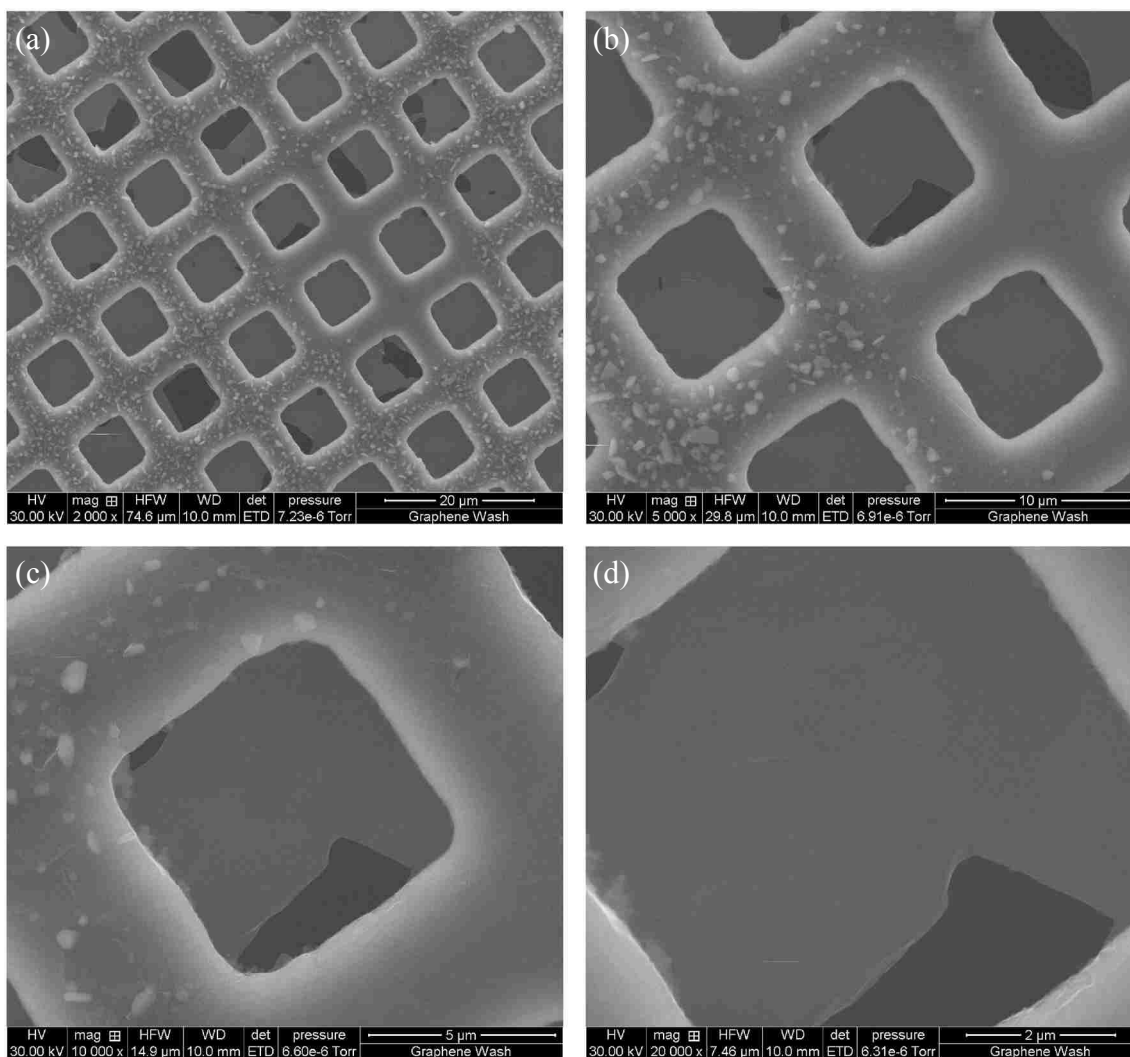


Figure 2: SEM images of freestanding graphene on a 2000-mesh, copper grid. Acquired using an FEI Quanta 200 field-emission SEM equipped with a scanning TEM detector and an Oxford INCA 250 silicon-drift, energy-dispersive X-ray spectrometer. Graphene covers most of the holes, but not the darker regions. Scale bars are included in the images.

B. IMAGING WITH ENHANCED CORRUGATIONS

Performing STM on a truly flexible substrate represents new territory, and as such, there was little framework for developing or interpreting the following experiments. Although numerous studies had used STM to image graphene at the atomic scale on various substrates, it was never certain that this would be possible with suspended graphene of any appreciable area. It had been attempted, but the system did not seem mechanically stable enough for such an ultra-sensitive technique [66]. Nevertheless, we sought to image the freestanding graphene as a starting point in order to establish its presence and character for any future research.

Experiment and Results

Constant-current STM images were acquired from both types of graphene sample, as shown in Fig. 3. Note that the hexagons in these STM images confirm that it is effectively single-layer graphene [67, 68]. All STM images presented are $400 \text{ pixels} \times 400 \text{ pixels}$ (400 data points per line with 400 lines per image) and have a black-to-orange-to-white color scale representing height. A representative $6 \text{ nm} \times 6 \text{ nm}$ STM image of graphene on copper foil is displayed in Fig. 3(a). The honeycomb structure is visible but somewhat obscured by the more dominant topography of the copper substrate. To see the graphene more clearly, the upper right inset shows an atomic-resolution image around a single honeycomb ring from the central section of Fig. 3(a). It is magnified two times and displayed with a compressed color scale. Below the STM image is a height cross-section line profile extracted across its center, showing an atomic-scale corrugation amplitude of about 0.05 nm . This is consistent with what is expected for stationary graphene [69].

A $6 \text{ nm} \times 6 \text{ nm}$ STM image of freestanding graphene is displayed in Fig. 3(b), but this was more difficult to obtain. While the STM can usually establish stable constant-current

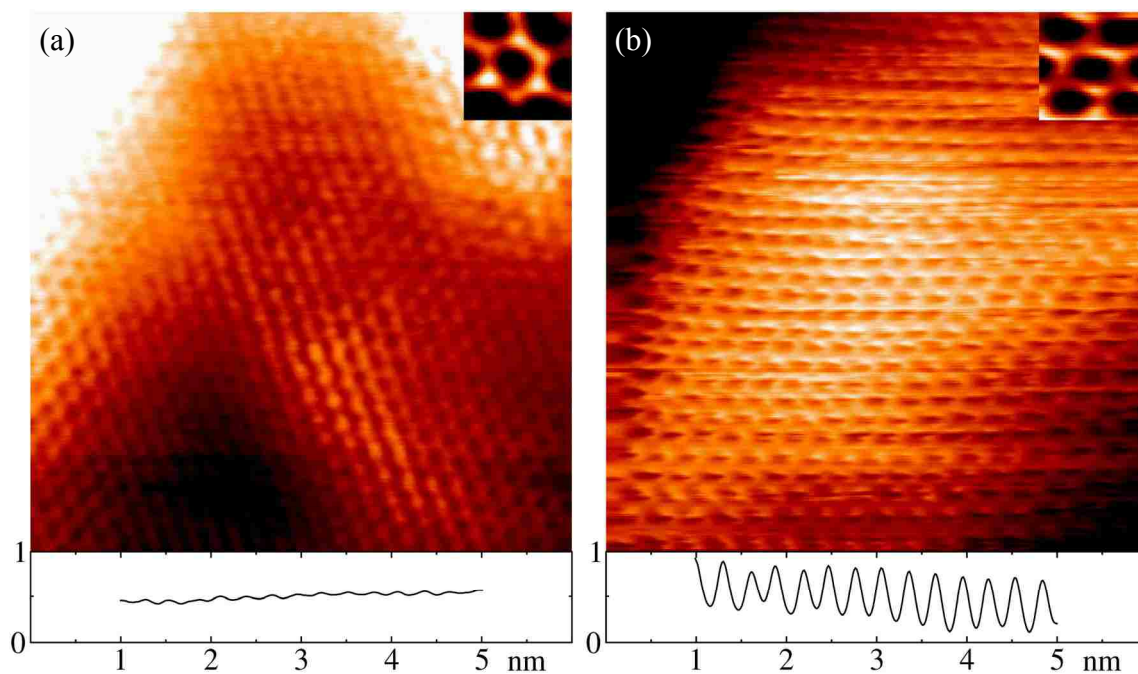


Figure 3: 6 nm \times 6 nm, filled-state STM images of (a) graphene on copper foil and (b) freestanding graphene. Imaging parameters were $V = 0.1$ V and $I = 1.0$ nA. The upper insets were cropped from their respective images, magnified two times, and displayed with compressed color scales. The lower graphs are height cross-section line profiles of the atomic corrugations, extracted across the centers of their respective images.

tunneling after approaching the freestanding graphene, it can rarely be maintained once we attempt to acquire an image of any appreciable size. We succeeded at this location, however, and several others although only one example is shown. The honeycomb structure is visible but noticeably warped, presumably due to the instability of the membrane and not because the bonds are actually stretched. The inset reveals the details of the distorted local atomic structure. There is also a curvature to the overall topography, highest along a diagonal line from the lower left corner to the upper right corner. The most remarkable feature of this data is that the underlying atomic lattice is still visible even with an overall black-to-white height scale of 4 nm. This is possible because the height change across each atomic ring is nearly a full nanometer (see line profile below image), 20 times greater than the electronic corrugation for graphene on copper. Such a surprising result deserves careful consideration.

Discussion

Clearly, the tip height when imaging freestanding graphene does not merely represent an electronic surface of constant LDOS. There must actually be two features that contribute to the atomic corrugation amplitude in Fig. 3(b), one electronic and the other elastic. The electronic component is caused by the spatial variation in the DOS, which is normally observed with STM. For graphene on a substrate, this electronic height change is known experimentally and theoretically to be at most 0.05 nm [69]. The elastic component is caused by movement of the freestanding graphene through electrostatic attraction between the biased STM tip and grounded sample, as depicted in Fig. 4(a). (In a related point, evidence for elastic distortions in graphite has been previously reported [70].) After much debate, it was suggested that this attractive force must increase and decrease in registry with the local charge density, meaning that it causes the flexible substrate to move up and down in the same pattern as the electronic “height,” thus

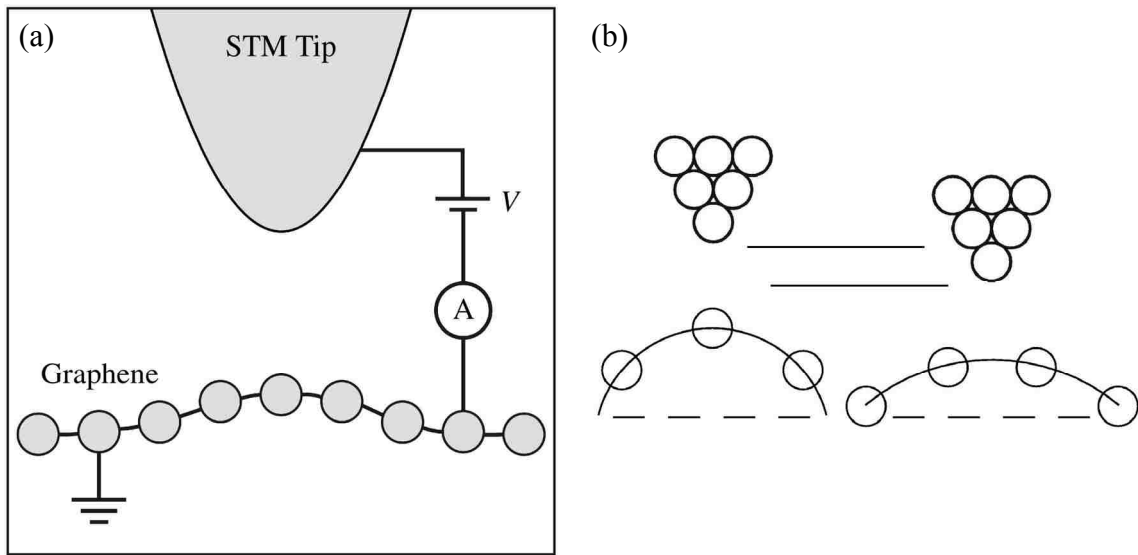


Figure 4: (a) Cross-sectional schematic of the STM tip in tunneling on suspended graphene using feedback-on electronics. The graphene is attracted to the tip due to an image charge.

(b) Diagram illustrating the tip over a carbon atom (left) and over a hole in the honeycomb lattice (right). The electrostatic attractive force is stronger and the graphene is pulled farther when over an atom, but the tip-sample separation remains approximately the same.

greatly enhancing the corrugations. This prediction was confirmed through a calculation using the self-consistent Hückel method, in which a point charge was placed 0.1 nm above a 20 nm × 20 nm graphene patch at different lateral locations [71].

To illustrate this interaction more clearly, imagine that the STM tip is brought into tunneling over a carbon atom, as shown on the left side of Fig. 4(b). The freestanding graphene is attracted to the tip by the electrostatic image force and moves toward it. The feedback circuitry retracts the tip until a sufficient elastic restoring force builds up in the graphene to balance the electrostatic attraction, and a stable tunneling current is achieved [71]. Next, as the tip scans away from the atom and toward the center of a hexagon, the electrostatic force decreases. Consequently, the elastic restoring force causes the graphene sheet to retract away from the tip, as shown on the right side of Fig. 4(b). The feedback circuit prompts the tip to chase the graphene about 1 nm until a new equilibrium configuration is reached and the tunneling current setpoint is restored. As the tip scans to the next atom, the electrostatic force increases once more, and the process repeats. This repetitive, dynamic, and interactive process is in perfect registry with the electronic corrugation, producing images which depict freestanding graphene at the atomic scale but with unexpectedly large corrugations.

C. CONSTANT-CURRENT ELECTROSTATIC MANIPULATION

Experiment and Results

The electrostatic attractive force between tip and sample can be studied and exploited using constant-current spectroscopy. Constant-height spectroscopy is not an option because the freestanding graphene will either crash into the tip or fall out of tunneling as the voltage is increased or decreased, respectively. Instead, the change in tip height required to maintain a constant current is recorded as the bias voltage is varied, as shown in Fig. 5 for suspended

graphene (top three pairs of curves) and graphene on copper foil (bottom curve). The inset shows the actual measured current versus voltage on a log scale. Notice that constant current is achieved, indicating that the sample and tip always maintain a close separation s to sustain electron tunneling. By doing the experiment with graphene on copper, we show that s changes by no more than a few nanometers due to the increased tunneling probability with applied voltage. Therefore, the much larger displacements attained with freestanding graphene must depend on movement of the sample, or else the tunneling current would decrease exponentially.

For the highest setpoint current, the freestanding graphene membrane rises and follows the tip about 30 nm as the voltage is increased to 3 V (solid red line). The result is almost fully reversible as the graphene drops by about 35 nm when the voltage is ramped back down (dashed red line). The graphene can be held at any height in between by simply setting the voltage accordingly. The setpoint current appears to play a similar role in the maximum displacement achieved. A tenfold reduction in current reduces the maximum height achieved by about a factor of 2. Therefore, a combination of setpoint current and bias (for fine tuning) can be employed to set the height of the graphene membrane at will. This electrostatic manipulation technique is ideal for precisely quantifying the movement of the freestanding graphene since the voltage is incrementally changed in small amounts (~ 10 mV step size), and the acquisition waits for a long time (~ 3 ms) so that the feedback can stabilize before the current and new vertical position of the STM tip are recorded. Furthermore, the voltages are kept low enough to disregard field-emission resonance effects [72, 73].

Discussion

The origin of the movement of the freestanding graphene membrane can be explained via mechanisms similar to those previously discussed with imaging. First, as the voltage increases,

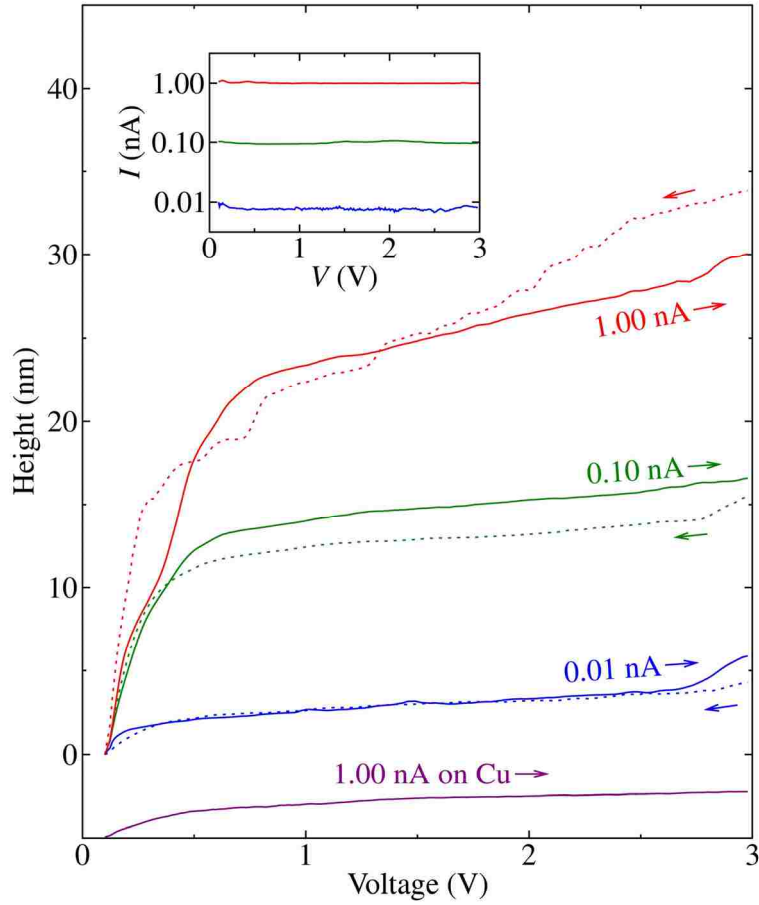


Figure 5: Constant-current STS data showing the vertical movement of the STM tip versus applied bias voltage for three different setpoint currents on freestanding graphene. The voltage was ramped both forward (solid lines) and backward (dashed lines). The bottom trace is graphene on copper data that has been offset for clarity. The inset shows the measured current on a log scale as a function of applied bias voltage during the corresponding STS measurements.

the current will increase due to an increasing tunneling probability. With the feedback turned on, the tip pulls away from the surface. However, the tip need only move about 0.1 nm to decrease the current by a factor of 10, so this portion of the movement will always be small [56, 69]. More relevant to this study, the increased bias voltage increases the electrostatic force on the freestanding graphene membrane, causing it to move toward the tip. To maintain a constant current, the tip pulls away from the approaching graphene membrane. The graphene continues to chase the tip until an elastic restoring force grows and eventually equals the electrostatic force [71]. At this point, an equilibrium is reached, allowing the system to achieve the setpoint tunneling current and record the new height. However, if the force is governed mainly by the voltage, one would expect each trial to reach the same final height regardless of the setpoint current. In the graph of Fig. 5, each curve was set to zero height at its beginning for convenience, but the sample does not necessarily begin at the same height each time. This important question will be revisited later.

It is interesting to notice that the curves are generally characterized by a quick rise as the tip bias is ramped from 0.1 V to around 1.0 V, followed by a plateau region over the remaining range to 3.0 V. This may be evidence of large-scale, low-energy configurations, or ripple textures, of the graphene membrane [17, 39, 74]. That is, the first linear region is soft due to removing ripples or slack, and the second region is harder due to straining the lattice. Insights like this make electrostatic manipulation of freestanding graphene a potentially valuable tool for learning about the elastic and electronic properties of freestanding graphene, especially when modified by local defects or nanoparticles [75, 76]. This experiment also demonstrates that STM can be used to induce a controllable strain on freestanding graphene membranes, laying the groundwork for using local probes in strain engineering [77, 78]. In fact, a number of studies

have employed the electrostatic STM force to test and manipulate freestanding graphene for various purposes [79-81], but they do not focus on elucidating the fundamental interaction.

D. IMAGE-CHARGE MODEL OF ELECTROSTATIC ATTRACTION

Setup and Derivation

In many ways, the $Z(V)$ results above would be more useful if one knew the electrostatic force F that the tip exerts on the sample as a function of bias voltage. While this is impossible to know exactly, we can calculate an approximate force using an idealized model. Let the STM tip be simplified to a conducting sphere of radius a , held at potential V , and placed with its outer surface a distance s from an infinite grounded conducting plane representing the graphene sample, as illustrated in Fig. 6. The resulting electrostatic problem has an exact solution found using the iterative method of images technique [82-84]. Because a point charge generates spherical equipotentials, the boundary condition on the sphere can be easily satisfied by removing the physical surface and placing a point charge of magnitude $q_0 = 4\pi\epsilon_0 aV$ at the former center of the sphere. Next, to satisfy the grounded boundary condition at the plane, an equal and opposite charge $-q_0$ must be placed equidistant from the plane and on the other side (see Fig. 6). Now the boundary condition on the plane is satisfied, but that on the sphere is no longer satisfied. Another positive charge of lesser magnitude must be placed inside the spherical boundary at a different location to satisfy the spherical equipotential again, followed by another opposite charge across the plane. As the iterations proceed, the magnitudes of the charges decrease so that only a finite number of image pairs (e.g., 40) needs to be considered for an accurate estimate. For illustration, three such pairs are shown in Fig. 6.

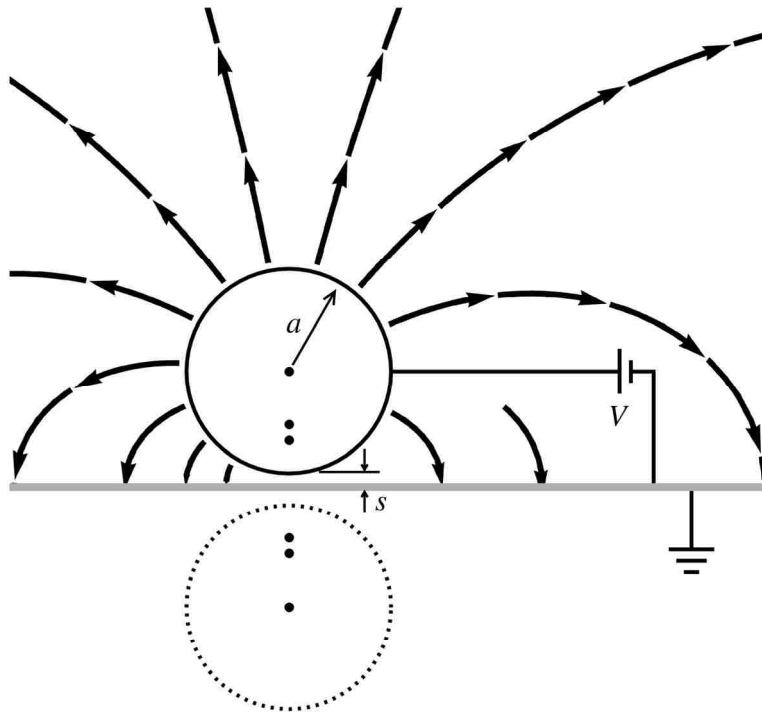


Figure 6: To-scale diagram illustrating the iterative method-of-images technique described in the text to approximate the tip-sample system and calculate the electrostatic attractive force. Calculated electric field lines are shown leaving the biased conducting sphere (STM tip) and ending at a grounded plane (graphene sample).

To determine the electrostatic attractive force between the tip and sample from the equivalent method-of-images construction, one must first compute the energy stored in the system. The electrostatic energy of the $N + 1$ positive charges in the upper half-plane is given by

$$U = \frac{1}{2} \left(q_0 + \sum_{i=1}^N q_i \right) V \quad (3)$$

where

$$q_i = \left(\frac{a}{x_0 + x_{i-1}} \right) q_{i-1} \quad (4)$$

is the magnitude of the i^{th} charge in the upper half-plane. Meanwhile, $x_0 = a + s$ is the position of the initial charge at the sphere center, and

$$x_i = x_0 - \frac{a^2}{x_0 + x_{i-1}} \quad (5)$$

is the position of the i^{th} charge measured relative to the plane. Because the plane is grounded, the electrostatic energy of the charges in the lower half-plane is zero, and the above expression is the energy of the entire system. The attractive force F between the sphere and plane is then given by

$$-\frac{\partial U}{\partial x_0} = -\frac{V}{2} \sum_{i=1}^N \frac{\partial q_i}{\partial x_0} = -2\pi\epsilon_0 a V^2 \sum_{i=1}^N \frac{\partial Q_i}{\partial x_0} \quad (6)$$

where $Q_i \equiv q_i/q_0$. The last step is performed in order to pull out the common q_0 factor and thereby show that the force is predicted to increase quadratically with the tip bias.

Since the electrostatic force depends quadratically [85] on the bias voltage ($F \propto V^2$), we can get a quick idea of how that force varies with tip height by plotting V^2 as a function of Z . This has been done for a new 1.00 nA $Z(V)$ curve, as shown in the main graph of Fig. 7(a). (The original data is provided in the inset.) The main plot is divided into four regions for discussion purposes: (I) low-bias voltages where $V^2 < 0.1 \text{ V}^2$, (II) voltages between 0.1 V^2 and 1 V^2 ,

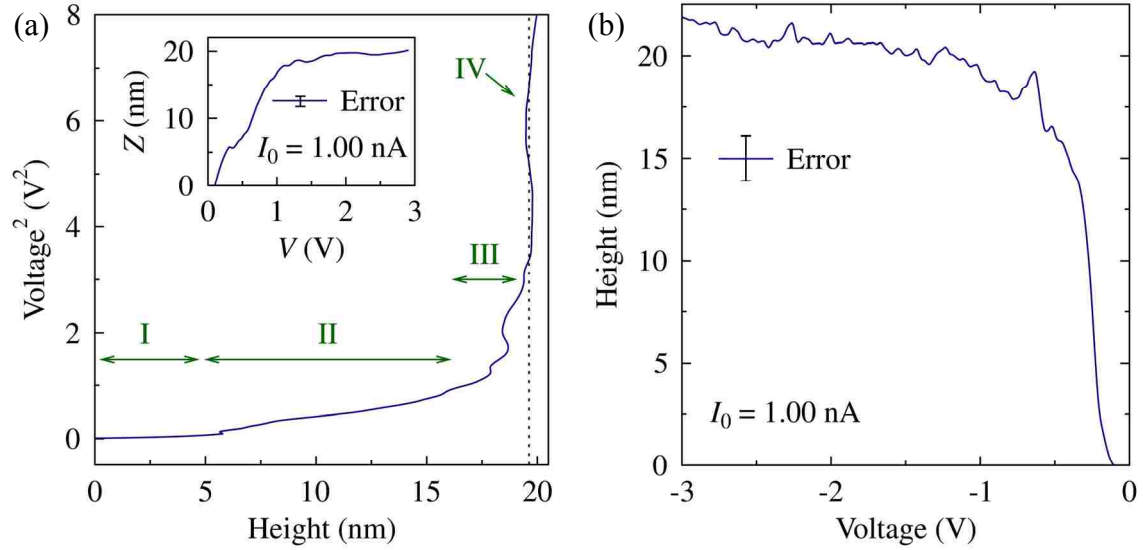


Figure 7: (a) The change in STM tip height at one location on freestanding graphene as a function of bias voltage. It increases by 20 nm as the voltage is ramped from 0.1 V to 3.0 V at 1.00 nA, as shown in the inset. The main plot is rescaled to show V^2 as a function of height because V^2 is proportional to the electrostatic force. The four regimes present in the data are: I) thermal fluctuations, II) linear elasticity, III) nonlinear elasticity, and IV) boundary effects. (b) Similar to (a) except that the voltage is decreased from -0.1 V to -3.0 V. The tip height still increases by about 20 nm (rather than decreasing) because the electrostatic force is proportional to V^2 . The error bars represent the standard deviation of ten repeated measurements taken consecutively at the same location of the sample.

(III) voltages between 1 V^2 and 4 V^2 , and (IV) voltages beyond 4 V^2 . In region (I) where the film has not been pulled very high, most likely the thermal contribution to the energy is much larger than the electrostatic one. After that, in region (II) where most of the height change happens, the electrostatic force is proportional to the height variation, and the system obeys Hooke's law (linear region). Next, in region (III) the electrostatic force is no longer proportional to the height variation, and the nonlinear effects become important. Finally, in region (IV) there is no further increase in the height with increasing voltage, meaning the graphene sheet is fully pulled up (i.e., tense membrane boundary condition) and becomes inflexible. One other important result of the $F \propto V^2$ conclusion is that similar height curves should be obtained whether positive or negative tip biases are used. The electrostatic force will still be attractive. The $Z(V)$ data in Fig. 7(b) was taken using the same parameters as that in Fig. 7(a) except that the voltage was decreased from -0.1 V to -3.0 V rather than increased from 0.1 V to 3.0 V . It demonstrates that the sign of the tip bias in fact does not influence the outcome.

Calculation of Force as a Function of Voltage

To put a number on the electrostatic force exerted by the STM tip as a function of bias voltage, we need to know the tip radius a and the tip-sample separation s to substitute into the equations derived from the sphere-plane model. This quantitative relationship has been plotted in Fig. 8(a) for several experimentally reasonable values of a and s , and over the voltage range used in our experiments. For clarity, the $s = 0.5 \text{ nm}$ and $s = 1.0 \text{ nm}$ families of curves are offset upward by 15 nN and 5 nN , respectively. We find that the largest forces are generated by a smaller s and larger a , with a maximum of 25 nN possible within the chosen parameter space. From several SEM images taken in other studies on electrochemically-etched tungsten STM tips, our best estimate for a realistic tip radius is $a = 20 \text{ nm}$ [86]. Similarly, from first-principles STM

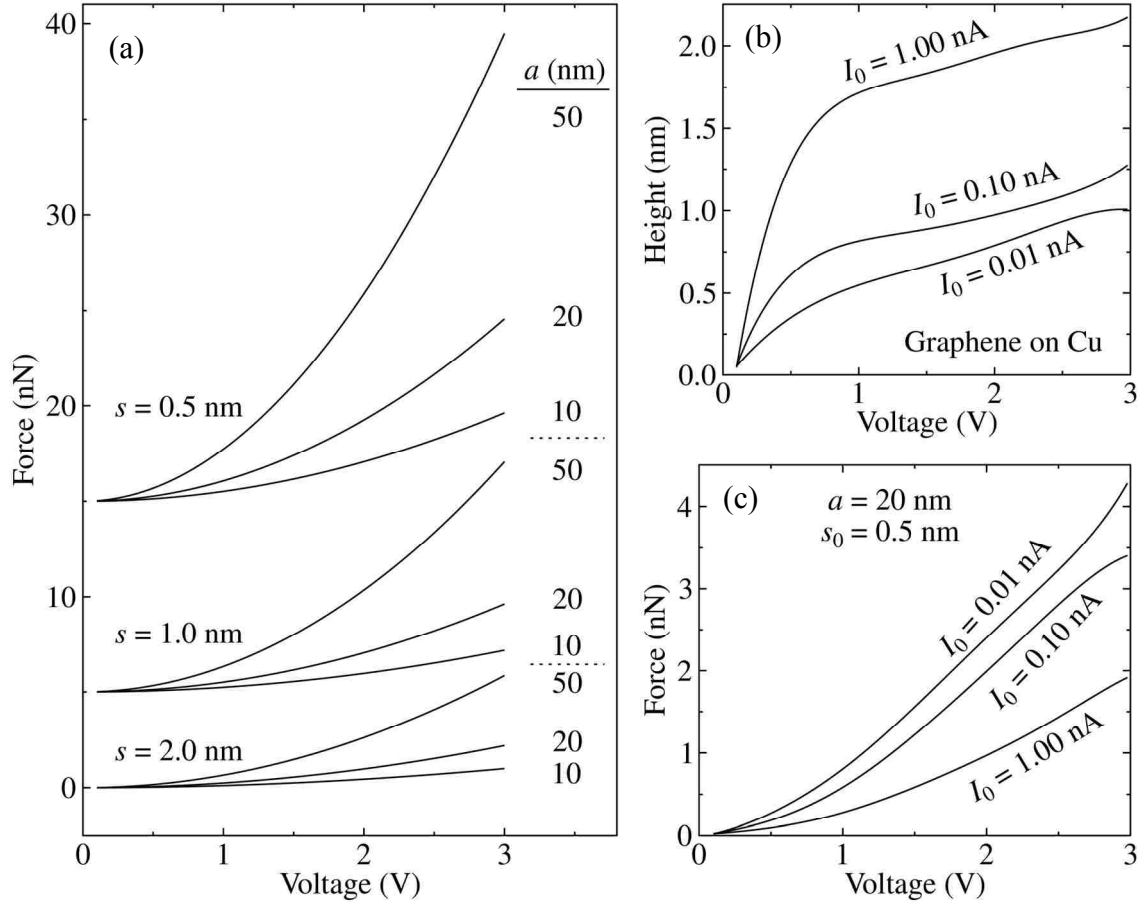


Figure 8: (a) Theoretical electrostatic sphere-plane forces as a function of the sphere potential for multiple sphere radii a and sphere-plane separations s . The curves for $s = 1.0$ nm and $s = 0.5$ nm have been offset upward by 5 nN and 15 nN, respectively. (b) Experimental $Z(V)$ curves at three different setpoint currents for graphene on copper foil (used to determine how s changes with V). (c) Corrected force curves, letting s begin at 0.5 nm and changing with V according to the data in part (b), and letting $a = 20$ nm.

tunneling studies [69], we conclude that a good average tip-sample separation in these experiments is $s = 1.0$ nm. These particular parameters give rise to a maximum force of about 5 nN.

Up to this point, however, our model neglects the small changes in the tunneling junction width which are known to occur as the tip bias is varied. These small changes can have a noticeable impact on the electrostatic force. To correct for this, experimental $Z(V)$ curves were acquired for graphene on copper foil, and are shown in Fig. 8(b). These measurements were performed in exactly the same manner as the earlier $Z(V)$ data for freestanding graphene, and in fact, the two sets of curves bear a strong resemblance. In this case, though, the graphene is bonded to the copper [31], preventing mechanical movement of the sample, so the tip displacements d_e are almost if not entirely electronic. Therefore, they are an order of magnitude smaller than those shown earlier in Fig. 5. The initial tip-sample separation s_0 in these experiments is still unknown, so we define the true $s(V) = s_0 + d_e$. This relationship is then assumed to hold for the freestanding graphene, so that in the above equations $x_0(V) = a + s(V)$, and at each V a new set of image charges is generated. Since the q_i/q_0 terms now vary with V , the $F(V)$ relationship is no longer purely quadratic. Three corrected $F_c(V)$ curves using $a = 20$ nm and $s_0 = 0.5$ nm are shown in Fig. 8(c). These are the final curves used to predict the electrostatic force as a function of bias voltage for our three setpoint currents. However, they could still use further revision since s_0 will not be the same for different tunneling currents. This may be responsible for $I_0 = 1.00$ nA yielding the lowest force although it should correspond to the smallest value of s .

E. LARGE PSEUDOMAGNETIC FIELDS

The discovery of graphene was made even more exciting when mechanical distortions were found to alter its electromagnetic characteristics. Through strain of the two-dimensional plane, the properties of charge carriers in graphene can change dramatically as gauge fields (pseudomagnetic and deformation potential) are created [87, 88]. For example, when uniaxial strain is applied to the honeycomb lattice, it affects the hopping probability for electrons in the p_z orbitals. The resulting energy change can be represented mathematically by a position-dependent vector potential, thereby suggesting the presence of a magnetic field [8]. Further analysis clarifies that it is in fact a pseudomagnetic field because opposite Dirac cones are related in such a way as to preserve global time-reversal symmetry. Guinea *et al.* predicted that this field should, nevertheless, have a measurable impact [89]. Experimental verification came from Levy *et al.*, who grew graphene on a platinum substrate [90]. After cooling to ~ 7.5 K, the graphene formed triangular nanobubbles due to its negative thermal expansion coefficient [39]. STS was then performed on the nanobubbles, and a series of peaks in the spectra was attributed to Landau levels originating from static magnetic fields with magnitudes as high as 300 T. Theoretically, such fields also form when the STM tip is used to pull on freestanding graphene. Since they cannot be measured directly, several steps are required to estimate the pseudomagnetic field strength present in our system. I do not develop a complete method here, but I provide the details related to certain necessary elements.

Shape of the Graphene Membrane

The first requirement is to know the shape of the graphene membrane when undergoing electrostatic manipulation by the tip. Since our displacements are very small relative to the sample size, the $7.5\text{-}\mu\text{m}$ -square boundary region can be reasonably approximated as circular,

with the tip pulling on a point at the center with a force F perpendicular to the plane. This particular setup is addressed in Ref. [91] using molecular mechanics simulations and von Kármán plate theory, but for small deflections the governing equations reduce to the Kirchhoff plate theory. An analytical expression can then be written for the vertical deflection w of the sheet as a function of the radial coordinate r . However, these are divided by the radius R of the graphene sample to express the equation with dimensionless quantities, $W = w/R$ and $\eta = r/R$. Specifically,

$$W(\eta) = \frac{P}{2\pi\lambda^2} \left\{ \frac{[I_0(\lambda\eta) - I_0(\lambda)] \times [1 - \lambda K_1(\lambda)]}{\lambda I_1(\lambda)} + K_0(\lambda) - K_0(\lambda\eta) - \ln \eta \right\} \quad (7)$$

where $P = FR/D$ is the dimensionless force, $\lambda^2 = N_0 R^2/D$ is a quantity determined by the initial in-plane tension N_0 , and D is the flexural or bending rigidity. In addition, I and K are the modified Bessel functions of the first and second kind, respectively. (Note that I does not refer to tunneling current in this context.)

Unfortunately, certain problems arise in attempting to apply this formula to the experimental freestanding graphene system. One difficulty is computational. When R is large, λ is very large, and $I_n(\lambda)$ quickly exceeds the maximum double-precision floating-point number. Luckily, for large, real arguments there is an asymptotic expansion [92]:

$$I_n(x) \sim \frac{e^x}{\sqrt{2\pi x}} \left[1 - \frac{4n^2 - 1}{8x} + \frac{(4n^2 - 1)(4n^2 - 9)}{2!(8x)^2} - \frac{(4n^2 - 1)(4n^2 - 9)(4n^2 - 25)}{3!(8x)^3} + \dots \right] \quad (8)$$

Since $I_0(\lambda\eta)$ and $I_0(\lambda)$ are both divided by $I_1(\lambda)$ in Eq. (7), the large exponential factor will be reduced, allowing the ratio to be computed even if the individual functions cannot be evaluated. MATLAB code for dividing two modified Bessel functions of the first kind with large arguments

can be found in Appendix A. A more challenging obstacle in determining the graphene shape is that the initial in-plane tension N_0 is unknown. In fact, it is likely that the membrane is rippled and not properly taut at the beginning of a given $Z(V)$ measurement [93, 94]. This means calculated pseudomagnetic fields should probably be viewed as upper limits. Furthermore, the appropriate flexural rigidity D is difficult to ascertain for the same reason, though many studies have sought to measure or predict it under more ideal circumstances [95-98]. These issues aside, an example of the possible graphene shape from Eq. (7) is depicted in Fig. 9, assuming $R = 3.75 \mu\text{m}$, $F = 5 \text{ nN}$, $D = 7.1 \text{ eV}$ (Ref. [95]), and $N_0 = 1.2 \text{ eV/nm}^2$ in order to attain a deflection of 30 nm at the center. The MATLAB generating code may be found in Appendix B.

Calculation of the Strain-Induced Field

If a 2D strain field \mathbf{u} can be obtained for the graphene sheet in polar coordinates (r, θ) , Ref. [89] provides general equations for the gauge-field vector potential \mathbf{A} and strain-induced pseudomagnetic field B . Assuming circular symmetry and a central point load (as in our system), $u_\theta = 0$ and $\partial u_r / \partial \theta = 0$. The given equations for \mathbf{A} thus reduce to

$$\begin{aligned} A_r &= \frac{\beta}{a} \left[\left(\frac{\partial u_r}{\partial r} - \frac{u_r}{r} \right) \cos 3\theta \right] \\ A_\theta &= \frac{\beta}{a} \left[\left(\frac{u_r}{r} - \frac{\partial u_r}{\partial r} \right) \sin 3\theta \right] \end{aligned} \quad (9)$$

(given in units $\hbar/e \equiv 1$) where a is the lattice constant of graphene (not a radius in this context), $\beta = -\partial \ln t / \partial \ln a \approx 2$, and t is the nearest-neighbor hopping parameter. Substituting these components into the equation for B yields

$$B(r, \theta) = \frac{\beta}{a} \left[\frac{\partial^2 u_r}{\partial r^2} - \frac{3}{r} \frac{\partial u_r}{\partial r} + 3 \frac{u_r}{r^2} \right] \sin(3\theta) = B(r) \sin(3\theta) \quad (10)$$

Corresponding code to calculate $B(r)$ from u_r is included in Appendix C. To get an idea of the induced pseudomagnetic field as a function of height on the electrostatically manipulated

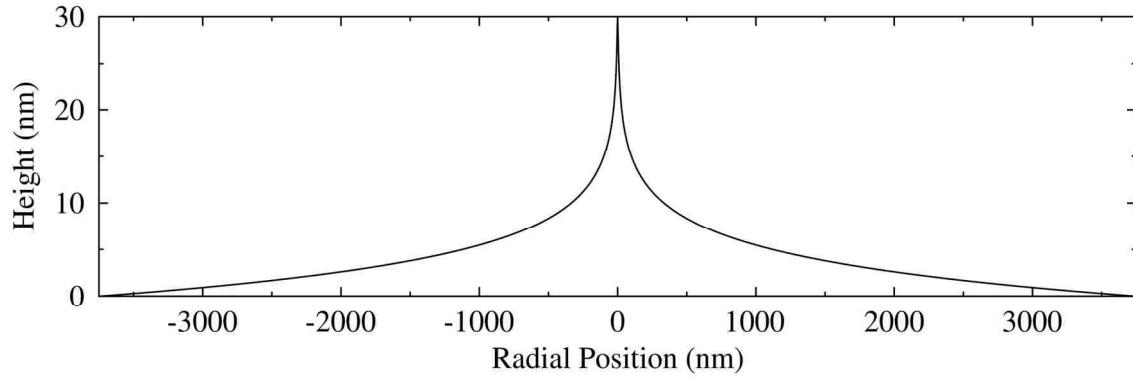


Figure 9: Shape of a circular freestanding graphene membrane under a central point load, using Eq. (7) and parameters listed in the main text. Note that the vertical dimension has been greatly exaggerated compared to the horizontal scale.

freestanding graphene samples, the above formulas were used in combination with the deformation potential from Ref. [99]. $|B(r)|$ was averaged from $r = 0$ nm to 5 nm, and this average was found to increase linearly to a maximum of about 25 T as $w(0)$ was raised to approximately 30 nm, as in the experimental data [71].

F. EFFECTS OF TUNNELING CURRENT ON GRAPHENE HEIGHT

Experimental Results and Discussion

Thus far, attention has been focused on varying the STM tip bias to apply a perpendicular electrostatic attractive force to the freestanding graphene sheet. However, it has already been observed that the tunneling current also has an effect on the height measurements. In order to systematically study this contribution, constant-bias $Z(I)$ measurements were taken for several voltage setpoints (V_0), as displayed in Fig. 10. These were performed with the feedback on, in the same manner as the earlier $Z(V)$ experiments, and each curve is again arbitrarily offset to have a height of zero at the starting current of 0.01 nA. In contrast with the $Z(V)$ measurements, the tip height decreases over the scan rather than increasing. Interestingly, a small V_0 (0.1 V) results in a very large initial drop of approximately 15 nm from 0.01 to 0.10 nA, followed by a slower decrease spanning more than 5 nm as the final current of 1.0 nA is approached. At high biases ($V_0 \geq 1$ V), on the other hand, the tip height decreases only a few nanometers or less, appearing almost constant by comparison, and the curves for intermediate voltages fall somewhere between these two extremes. The inset, showing the measured tunneling current (I) plotted versus the setpoint current (I_0), confirms that the tunneling current setpoint was continuously maintained throughout the scans.

The origin of the downward movements is not immediately obvious. In order to increase the tunneling current, the tip would move toward the sample as observed. However, the

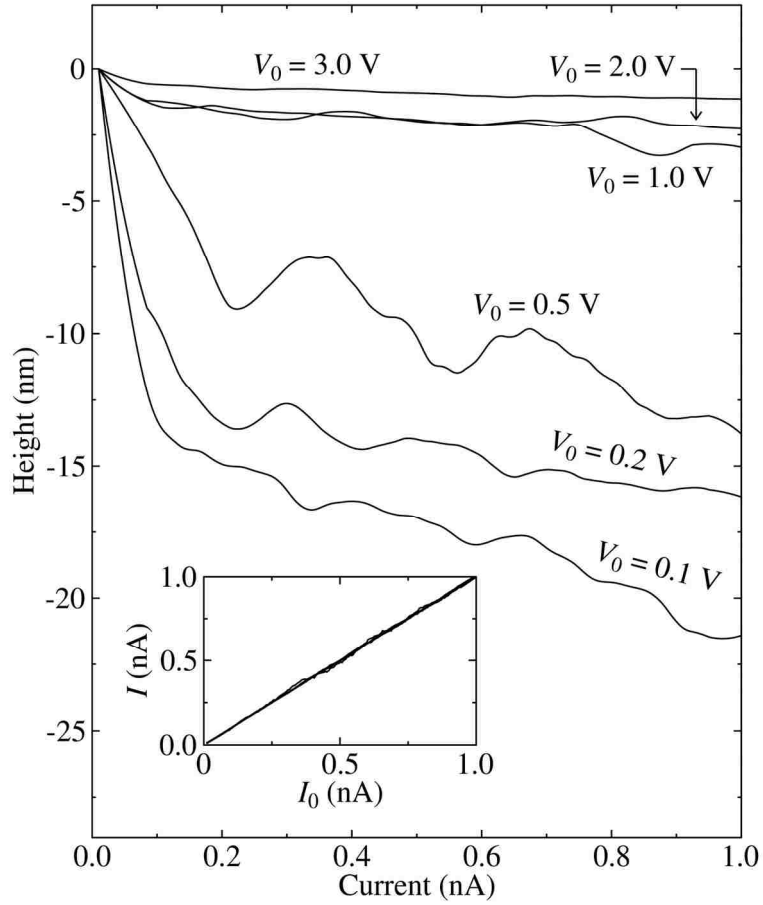


Figure 10: Tip height versus tunneling current for six different constant voltages on freestanding graphene. Inset confirms the measured current agreed with the setpoint as it was raised.

displacement at low voltage is too large to be purely a change in the tunneling gap. Moreover, decreasing the tip-sample separation would increase the electrostatic attractive force, which by itself would cause a height increase rather than a decrease. The remaining possibility to consider is that increasing the current locally heats the graphene [100], causing it to contract and pull away from the tip due to its negative thermal expansion coefficient. This contraction is not to be understood in terms of a decreasing bond length, but rather thermal excitations are known to increase the amplitude of out-of-plane atomic vibrations, which causes an effective in-plane contraction [101-103]. At low voltage, this effect is stronger than the electrostatic force, resulting in a large downward displacement. At high voltage, on the other hand, the electrostatic force is dominant, and the sample is not allowed to contract much as the current is increased.

This revelation means an adjustment should be made to the $Z(V)$ graph in Fig. 5. Since the $Z(I)$ sample height is approximately the same across all currents when $V_0 = 3.0$ V, the $Z(V)$ curves, which all end at 3 V, should have nearly equal final heights rather than the same starting heights. A new but similar set of $Z(V)$ data has been plotted in Fig. 11(a) and offset using the 3-volt $Z(I)$ data shown in the inset. Note that the shift is also independently consistent with the $Z(I)$ data for lower voltages. This representation of the data naturally shows that the graphene film plateaus at nearly the same height, regardless of current, representing a taut graphene configuration. In other words, the graphene is not actually being stretched farther at larger currents as it previously appeared. Rather, it is starting at a lower position due to thermal fluctuations, and this is overcome as the voltage and electrostatic force are increased.

Additionally, the force curves earlier derived may now be combined with the corrected $Z(V)$ data to plot the force as a function of height, as in Fig. 11(b). The $F(Z)$ curves are approximately flat up to around $Z = 20$ nm, after which the force increases very rapidly, up to a

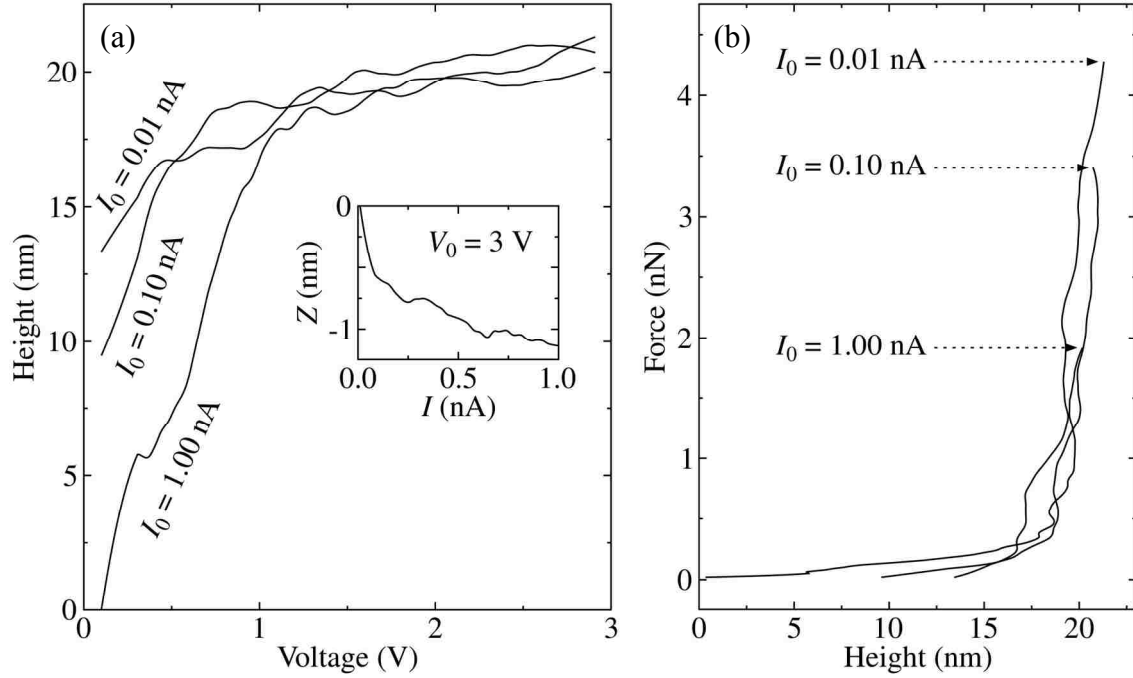


Figure 11: (a) New $Z(V)$ data, similar to that in Fig. 5 but offset to agree with the $Z(I)$ results in Fig. 10. The inset shows the 3.0 V curve used to set the final heights relative to one another.

(b) Force exerted on graphene by the tip as a function of height, deduced from the data shown in (a) and earlier sphere-plane electrostatic force calculations. Each curve roughly follows the same path.

maximum value (which is just over 4 nN for the $I_0 = 0.01$ nA curve). This indicates that the graphene is more flexible at first and suddenly becomes rigid, or that bond bending is primarily responsible for the large movements and not bond stretching. Also, each curve nearly overlaps the others, which suggests that the force necessary to bend the membrane a given amount in this region is largely independent of the tunneling current chosen. However, the starting height is directly affected by the tunneling current, and it decreases with increasing I_0 . Finally, the work done by the STM on the freestanding graphene for each trial can be calculated from the area under the curve, and it was found to be roughly the same for each at about 50 eV.

Modeling Thermal Contraction of Graphene

One simple model for understanding the contraction of the graphene membrane as the current is increased is illustrated in Fig. 12. A common statistical mechanics problem involves the average length and tension of a rubber band at various temperatures T and loads F [104]. The rubber band is modeled as a series of segments that can be oriented either parallel or antiparallel (details not shown in the figure) [105]. As the rubber band is heated, the segments favor an antiparallel arrangement, decreasing the total length and resulting in a negative thermal expansion coefficient. Quantitatively, the length of a rubber band carrying a constant load is proportional in first order to F/T (see Appendix D), where a larger F stretches the system and a larger T contracts the system. For our experiment, the tunneling current sets the temperature of the sample through Joule heating ($T \sim I^2$), so as the setpoint current is increased, the sample's local temperature is increased. We observe that the graphene contracts sharply at first and then more slowly, creating $Z(I)$ curves that qualitatively obey a $1/I^2$ relationship, like the one in Fig. 13. In this way, the rubber band model correctly mimics both the contraction of the graphene and the specific $1/T$ dependence. In addition, we can estimate the temperature of the

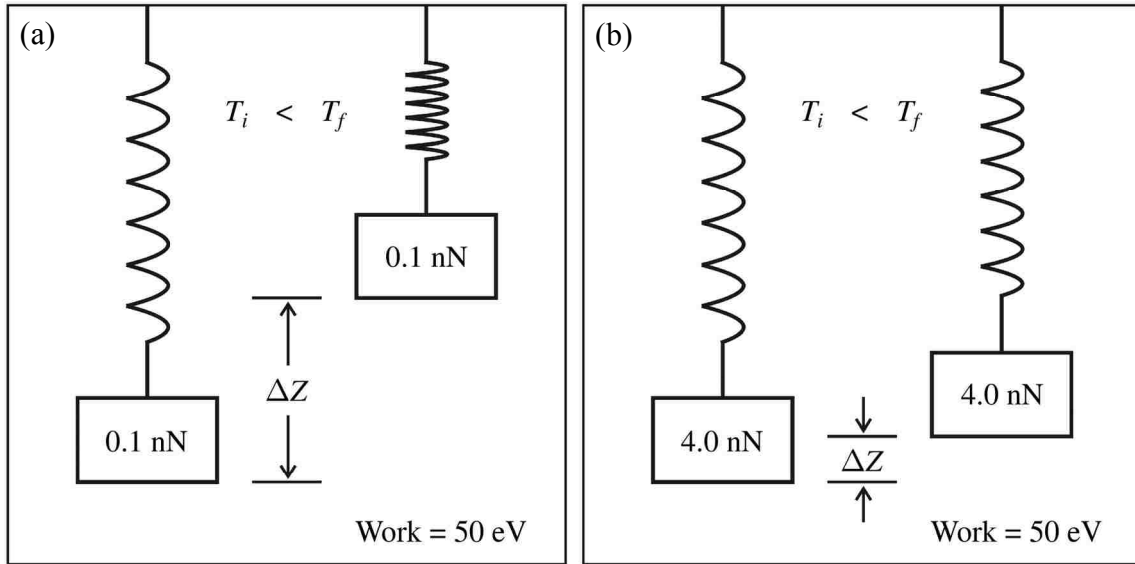


Figure 12: Schematic diagrams illustrating the entropic rubber band model, to which freestanding graphene is compared. The same change in temperature occurs in both, resulting in a larger displacement for the smaller weight and a smaller displacement for the larger weight (for the same amount of work done). In the STM, temperature is controlled by the tunneling current and weight, or force, by the tip bias.

graphene directly under the STM tip. Using a value of -10^{-5} K^{-1} for the thermal expansion coefficient, our height contraction of 20 nm, and assuming a distance of 3 μm to the copper support (which is held at room temperature), an increase of 10–100 K is estimated [39].

The rubber band model can also be used to explain the bias dependence of the $Z(I)$ measurements shown in Fig. 10. For the rubber band model, under a small load, it contracts a large amount ΔZ for a given increase in T , as illustrated in Fig. 12(a). However, when the load is increased, the length will change much less for the same temperature difference ΔT (and for the same amount of work done), as shown in Fig. 12(b). For our experiments, the bias voltage sets the load or force through electrostatics, so as the voltage increases the force increases. Thus, at low bias, the small force on the graphene allows a large displacement as the current is increased, whereas at high bias the large load on the graphene results in a much smaller displacement over the same increase in current or temperature.

A more quantitative approach can also be applied. As already mentioned, we assume that in the steady state, the temperature rise under the tip is proportional to the power of the Joule heating at the junction ($\propto I^2$). Then the local height of the graphene under the tip decreases as $h = h_0 e^{-kI^2}$ due to contraction, where $h_0 = h(I = 0)$ depends on V , while the constant k depends on graphene's thermal conductivity and expansion coefficient, as well as on the tip-sample separation $s = \frac{1}{2c} \ln(V/R_0 I)$ (see Appendix E for details). A typical value of the decay constant c is 1 \AA^{-1} , and the contact resistance R_0 is typically 13 k Ω . However, at constant V we can let $s = b \ln(I)$ and determine the unknown parameters by fitting the total tip height

$$\text{Height}(I) = h_0 e^{-kI^2} + b \ln(I) + z_{\text{offset}} \quad (11)$$

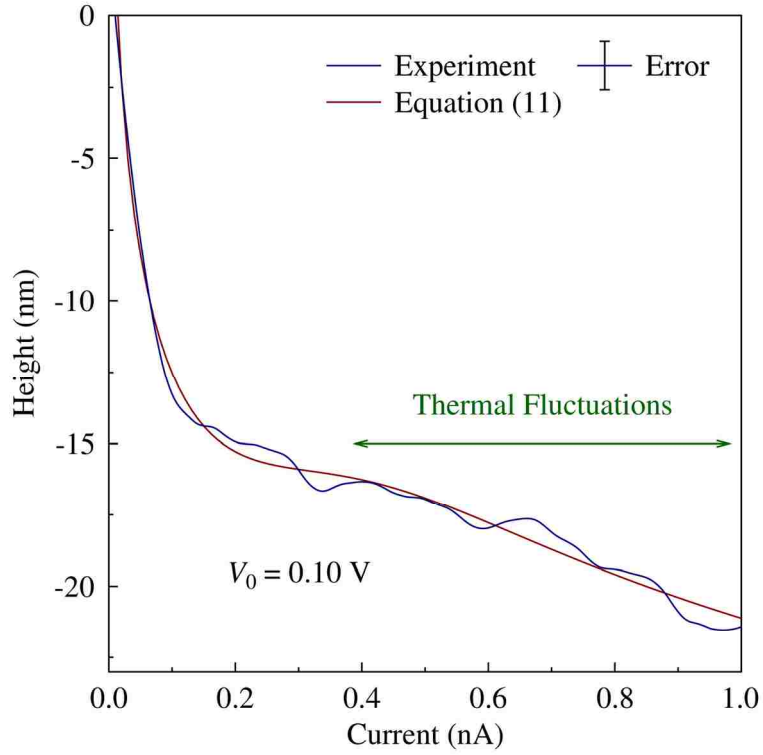


Figure 13: The change in STM tip height at one location on freestanding graphene as a function of tunneling current. The experimental height decreases by 20 nm as the current is raised from 0.01 nA to 1.00 nA at 0.1 V, and this behavior can be replicated by Eq. (11). Thermal fluctuations appear at higher currents. The error bar represents the standard deviation of ten repeated measurements taken consecutively at the same location of the sample.

to the experimental data. Doing so can replicate the shape of a $Z(I)$ curve very closely, as seen in Fig. 13. Note that the z -offset is necessary because the absolute starting height is unknown; it is set to zero in the graph for convenience.

IV. MEASURING LOW-FREQUENCY HEIGHT FLUCTUATIONS

Tracking the movement of individual atoms has its origins in field ion microscopy [106], but STM ushered in a new era. For instance, Mo *et al.* used STM to observe the migration of Si atoms on the Si(001) surface and extract the activation energy for diffusion [107].

Swartzentruber went a step further by programming the STM tip to physically follow each step of a single diffusing atom, thereby recording its site-to-site movement [108]. In this tradition, I now present a method using STM to precisely monitor the out-of-plane motions of a one-square-angstrom region in freestanding graphene for the first time. These fluctuations [109] are linked to the flexural phonon modes, which are critical to many of graphene's amazing properties, such as its previously unpredicted stability [16, 19], anomalous negative coefficient of thermal expansion [110], and efficient thermal conductivity [111]. The ripples which form as a result are also important for understanding transport properties in graphene, as they decrease the carrier mobility in freestanding membranes [112], cause disruptive charge puddling [113], and induce strong pseudomagnetic fields [8]. The ability to locally measure the thermal fluctuations as a function of time will open the door to directly testing their role in these and other important processes.

A. DEMONSTRATION OF EXPERIMENTAL TECHNIQUE

All fluctuation data was recorded by taking a $0.1 \text{ nm} \times 0.1 \text{ nm}$ STM image on freestanding graphene, such as the example shown in Fig. 14(a) (lower image). The scan rate was 0.2 nm/s , with 400 data points per line and 400 lines per image. For each line, the topographical data was collected simultaneously with the tunneling current in both the forward and backward scanning directions. In this way, each line took one second to complete for a total of 400 seconds per image. To understand the size of this scan relative to the lattice of atoms in graphene, refer to

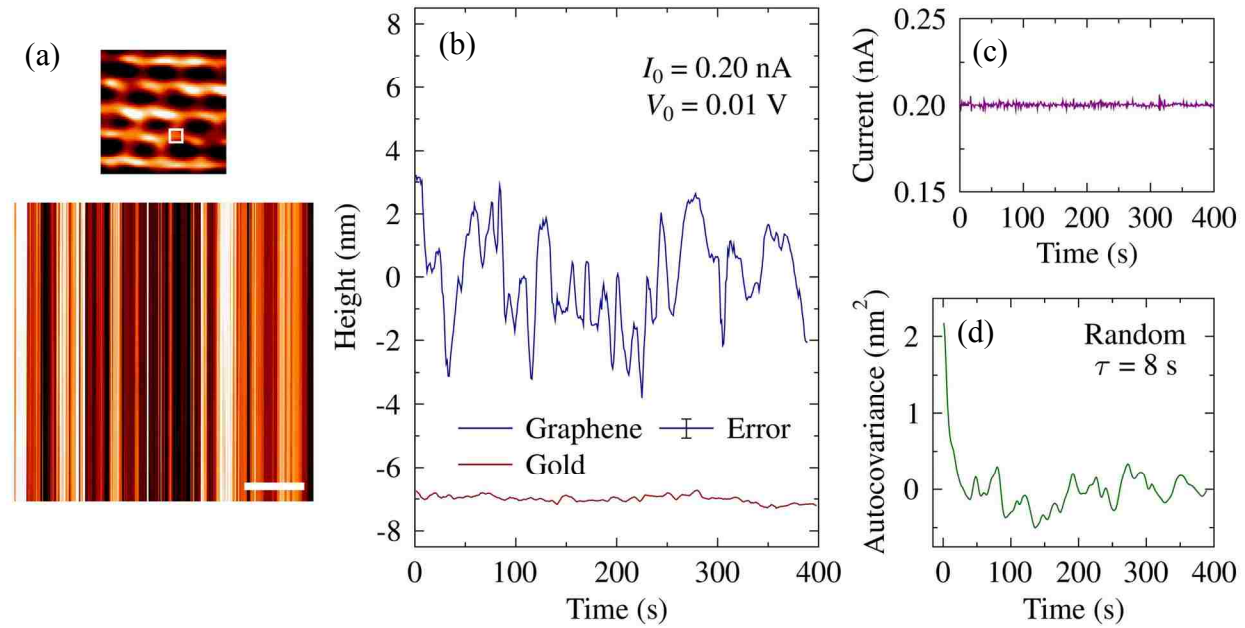


Figure 14: (a) Top: a $1 \text{ nm} \times 1 \text{ nm}$ filled-state STM image of freestanding graphene with a box highlighting the size of a one-square-angstrom region. Bottom: a one-square-angstrom STM image taken at constant current (0.20 nA) and voltage (0.01 V) on freestanding graphene, showing the height fluctuations over a time of 400 s . The slow scan direction is oriented horizontally. Scale bar, 0.02 nm . (b) Height fluctuations as a function of time, taken by averaging the points in each vertical line of the lower STM image. For comparison, the same data was collected from a sample of gold. The error bar represents the standard deviation of the 400 data points in the fast scan direction. (c) Actual tunneling current measured concurrently with the height fluctuations. (d) Autocovariance of the height data, with an exponential decay constant of 8 s .

the $0.1 \text{ nm} \times 0.1 \text{ nm}$ square outlined in the upper STM image, which was acquired separately from a stabilized region of the same freestanding graphene sample. The lower image shows the height of the tip in the normal black-to-orange-to-white color scale, but it is oriented such that the slow scan direction is horizontal and the fast scan is vertical. Note that significant changes in height rarely occur within a single vertical line. Therefore, a height-time signal was extracted along the slow scan direction by averaging the 400 points in each vertical line, resulting in a sampling frequency of 1 Hz over 400 s, as shown in Fig. 14(b). The unique power of this technique is that it effectively monitors the vertical position of a one-atom sized region for a long period of time. Normal imaging covers too large an area to determine how any one location changes on a short timescale, and spectroscopy measurements like those in Fig. 5 happen too quickly to observe these fluctuations, though focused in one spot.

The result on freestanding graphene is that the height displacements greatly exceed the scale of the scan area. In this low-bias regime (0.01 V), thermal energy is dominant. The graphene height in Fig. 14(b) fluctuates around zero (average height was subtracted from the raw data) with a standard deviation of 1.47 nm, an indication of the amplitude of wrinkles present in the graphene. For comparison, data taken in exactly the same manner on a sample of gold is also plotted, showing only the smallest changes in height over the entire scan. In addition, we always verify that the graphene is indeed moving with the tip by measuring the tunneling current as a function of time, displayed in Fig. 14(c). It is almost constant at the setpoint value (0.2 nA), and the variations that do occur are not large enough to account for 3-nm fluctuations in the tip height without the sample also moving. We can further characterize each height-time data set by calculating its autocovariance function $A(t)$ (defined in Appendix F), which is plotted in Fig. 14(d). $A(t)$ decays exponentially for random fluctuations such as these, indicating that they

are only correlated for short periods of time. In this example, the decay constant is 8 s. Atomistic simulations for the scaling properties of flexible membranes predict [114] that the size of the fluctuations of thermal ripples in freestanding graphene is scaled with the size of the system as $0.00232L^{2-\eta}$, where $\eta = 0.85$ is a measure of the anharmonic effect in graphene. It is noteworthy that the height variance of 2.17 nm^2 observed in Fig. 14(b) is in reasonable agreement with that prediction.

B. PERIODIC FLUCTUATIONS

Data and Analysis

When we increase the tunneling current, the freestanding graphene exhibits noticeable periodic oscillations as represented in Fig. 15. The electronics (cabling and pre-amplification in particular) used for these experiments effectively act as a low-pass filter with a bandwidth (-3 dB) of approximately 800 Hz. In addition, the speed at which we acquire digital data is 800 points per second, so we have a maximum measurable frequency of 800 Hz. And for the height-time graphs presented here, digital data was collected for 400 s, giving a minimum detectable frequency of 0.0025 Hz. Two typical samples of height-time data, taken at different currents but at the same location and the same low voltage (to avoid stretching), are displayed in Fig. 15(a). The most noticeable difference is in the peak-to-peak amplitude; however, the fluctuations in both appear to have a roughly repeated character.

The periodic components of the data were confirmed by calculating $A(t)$ for each curve, plotted in Fig. 15(b). Its peaks share the periodicity of the signal, which is clearly around 100 s at 3 nA and 50 s at 5 nA. Conveniently, the linear susceptibility $\chi(t)$ can also be obtained from $A(t)$ according to

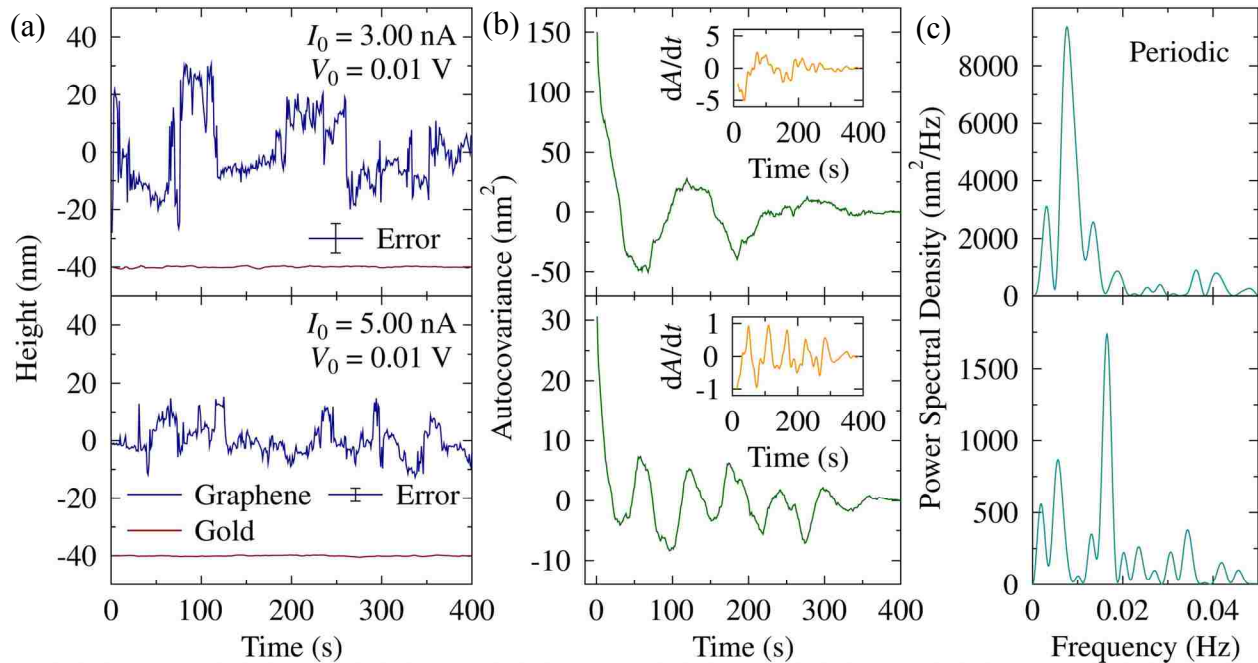


Figure 15: (a) Four line profiles taken in the same manner as those in Fig. 14(b). All were acquired at a tip bias of 0.01 V, but the tunneling current was 3.00 nA for the top set and 5.00 nA for the bottom set. (b) Associated $A(t)$ for each graphene curve in part (a). This function shares the periodicity of the signal. Smoothed first derivatives (related to the linear response) were calculated using the Savitzky-Golay algorithm and are plotted as insets. (c) Power spectral density for each graphene curve in part (a), revealing the primary oscillation frequencies.

$$\chi(t) = -\frac{1}{k_B T} \frac{dA(t)}{dt} \quad (12)$$

where k_B is the Boltzmann constant, and T is the absolute temperature [115]. dA/dt is therefore plotted as an inset for each curve in Fig. 15(b) and gives a maximum susceptibility of 5 nm²/s. (The smoothed first derivatives were calculated using the Savitzky-Golay algorithm [116, 117]. I wrote an executable program in C++ for general Savitzky-Golay smoothing and derivatives, which is included in Appendix G.) Furthermore, $\hat{\chi}(\omega)$, the Fourier transform of $\chi(t)$, can in turn be related to the power spectral density $S(\omega)$ by the fluctuation-dissipation theorem, which states

$$S(\omega) = \frac{2k_B T}{\omega} \text{Im}[\hat{\chi}(\omega)] \quad (13)$$

where ω is the frequency. The periodogram, an estimate of $S(\omega)$ for a discrete, finite signal, was computed for the periodic results and plotted in Fig. 15(c). (The periodogram is defined in Appendix F, and MATLAB code for calculating it may be found in Appendix H.) The 3 nA periodogram spectrum has a prominent maximum near a frequency of 0.01 Hz, and gives a maximum power spectral density of 9,000 nm²/Hz. Meanwhile, the 5 nA spectrum peaks around 0.02 Hz, and gives a smaller maximum power spectral density of 1,500 nm²/Hz. These low-frequency peaks represent the dissipation of thermal energy through flexural acoustic modes near the Brillouin zone center [118-120].

At this point, it is worth comparing our findings with a previous study. The general topography of ripples in freestanding graphene was first imaged using STM by Zan *et al.* [121]. With a STM setup similar to ours, they found that the height of the ripples was on the order of 1 nm and that the wavelength was on the order of 5 to 10 nm. They also report that the ripple structure is static in time and is stable enough to repeatedly image the surface topography. At first, this seems to contradict our results. However, Zan *et al.* also report that the freestanding

graphene sheet has regions that are too unstable to image with the STM (i.e., when they look in a region far from the copper bar supports). This is also what we found. The surface of the graphene fluctuates too quickly for the STM to acquire constant-current images of the surface topography. However, we have been able to tunnel into the graphene sheet at that one spot, maintain a constant current, and record the height changes occurring in time. Sometimes the surface will spontaneously stabilize as shown in Fig. 3(b), and then, if it stays that way, it can be imaged with the STM. We also found that the surface can be locally stabilized using constant current height-voltage sweeps up to 3 V.

Agreement with Elasticity Theory

If we model the freestanding graphene sample as a doubly-clamped resonator with length $L = 7.5 \mu\text{m}$ and mass density ρ subjected to an initial strain ε , plate theory predicts a resonance frequency given by $f = \frac{1}{2L} \sqrt{\frac{Y}{\rho}} \varepsilon$, where $Y = 340 \text{ N/m}$ is the Young's modulus. This results in frequencies in the GHz range [122], which is much too large for our results. Therefore, in order to explain the experimental data using elasticity theory, a different mechanism must be invoked. Since the measurements in Fig. 15(a) are performed in the limit of high electric current (i.e., temperature) and low (but not negligible) bias voltage, there are additional terms in the stress tensor [123]:

$$\sigma_{ij} = 2\mu \left(\varepsilon_{ij} - \frac{1}{2} \delta_{ij} \sum_i \varepsilon_{ii} \right) + B \left(\sum_i \varepsilon_{ii} + \alpha \Delta T \right) \delta_{ij} \quad i, j = 1, 2 \quad (14)$$

where the Lamé coefficient μ characterizes the shear rigidity of graphene, $B = \frac{Y\mu}{4\mu - Y}$ is the bulk modulus [103], and $\alpha \approx 5 \times 10^{-6} \text{ K}^{-1}$ is the absolute value of the thermal expansion coefficient at room temperature. The last term represents the thermal stress due to the temperature gradient near the tip region and the supports. In the steady state, ΔT is constant for a given electric

current. In the presence of thermal stress, using Eq. (14) and the corresponding equation of motion for the graphene membrane results in the following flexural phonon frequency [124]:

$$\omega_q = q \sqrt{\frac{\kappa q^2 + \tau}{\rho}} \quad (15)$$

where κ is the bending rigidity of graphene, $\rho \cong 7.6 \times 10^{-7} \text{ kg m}^{-2}$ is the mass density, and $\tau = -B\alpha\Delta T$ is the effective negative surface tension. Since $\Delta T > 0$, Eq. (15) can result in low frequencies. The critical wave vector is determined as

$$q_c (\text{\AA}^{-1}) = \sqrt{\frac{|\tau|}{\kappa}} \quad (16)$$

Using typical values [112] of $\kappa = 1.1 \text{ eV}$ and $B = 208 \text{ N/m}$, we can estimate the critical wave vector, which attains realistic values for low ΔT . For example, at $\Delta T \simeq 10 \text{ K}$, $\Delta T \simeq 20 \text{ K}$, and $\Delta T \simeq 100 \text{ K}$ the corresponding wavelengths are around 26 nm, 18 nm, and 8 nm, respectively. Note that longer critical wavelengths would be expected when other external stress sources exist; for example, when scanning close to the boundary or in the presence of a strong asymmetry.

By defining $\gamma = q/q_c$, we can rewrite Eq. (15) as

$$\omega_q = \gamma \sqrt{(\gamma^2 - 1) \frac{\kappa}{\rho}} q_c^2 \quad (17)$$

And for q near to q_c , Eq. (17) results in small frequencies with $\omega_{q_c} \propto \Delta T \propto I^2$. Therefore, the larger the electric current, the larger the frequency when q is very close to q_c . This prediction is confirmed in Fig. 16(a) by plotting the primary oscillation frequency as a function of I^2 and a linear trend line for four different scans obtained at the same low bias voltage. Furthermore, we can deduce based on the aforementioned theory that the bottom panel in Fig. 15(a) is more

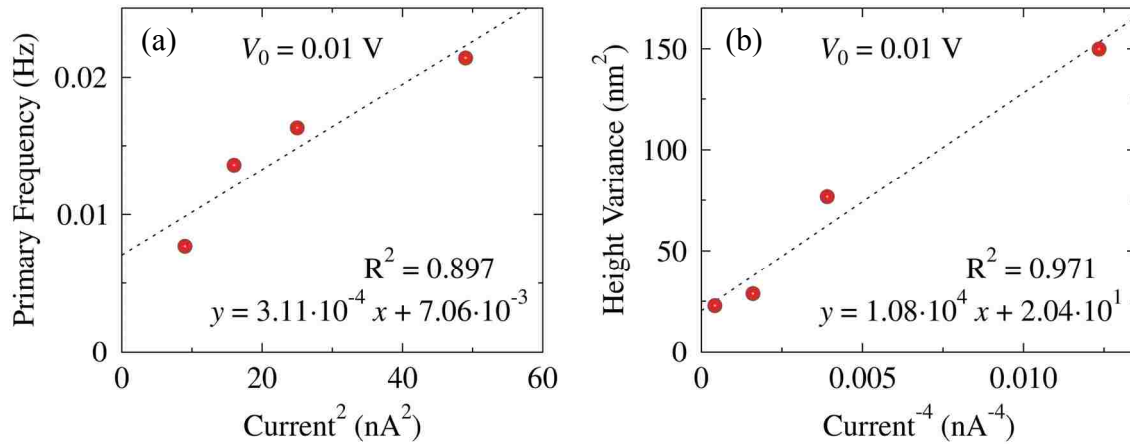


Figure 16: (a) The primary frequency as a function of I^2 for four height-time STM images of freestanding graphene taken with a tip bias of 0.01 V. A trend line has been added to demonstrate the linear relationship of the data. (b) The height variance as a function of I^{-4} for four height-time STM images of freestanding graphene taken with a tip bias of 0.01 V.

affected by thermal stress than the top panel. Also the height variance should approximately obey $\langle Z^2 \rangle \propto I^{-4}$ [124], which is in agreement with these four different electric currents as shown in Fig. 16(b). In fact, these results are evidence for the softening of flexural phonons in the case of compressive strain in graphene. This result has been theoretically predicted using density functional theory calculations combined with non-linear classical elasticity theory [110, 125].

C. MIRROR BUCKLING

A final type of fluctuations discovered appears to exhibit a “mirror buckling” effect and is explored in Fig. 17. The example STM image shown in Fig. 17(a) is very dark for the first fourth of the image and nearly white for the rest, signaling that a sudden jump has occurred which is much larger than the variations before or after. A height-time profile, extracted in the manner previously described, is plotted in Fig. 17(b) to reveal that the membrane surprisingly undergoes an enormous 60 nm displacement around $t = 100$ s but oscillates relatively little after the jump, somewhat similar to a critical transition. Examining the tunneling current as a function of time, as provided in Fig. 17(c), verifies that the sudden displacement is a real effect. Because the current is reasonably constant at 4 nA except for a spike coinciding with the jump in height, and since the spike is well below the system’s saturation current of 50 nA, tunneling was never compromised. Height profiles such as this yield an unusual $A(t)$, plotted in Fig. 17(d). It takes a much longer time to decay, and its value at $t = 0$ (equivalent to the variance $\langle Z^2 \rangle$) is anomalously large. This snap-through behavior can typically be produced by performing a series of scans at progressively larger currents, keeping the voltage constant. The Fig. 17 data was part of such a series that went all the way up to 10 nA. However, the large jump normally only occurs once as the current is increased within these limits, and not always at the same current.

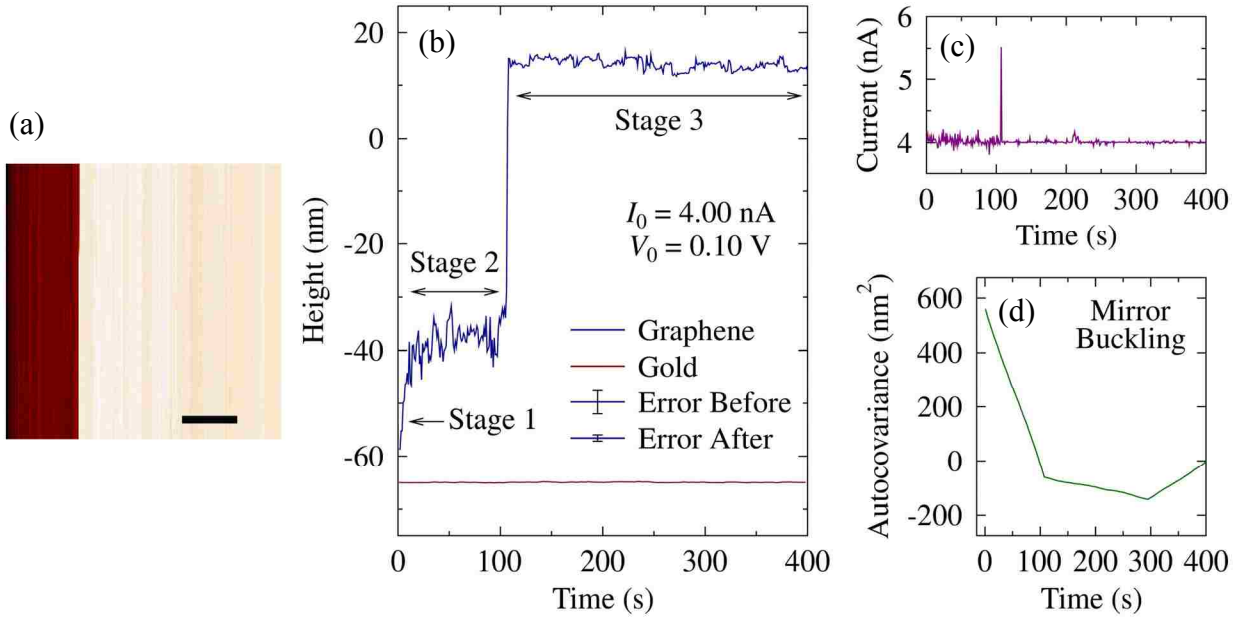


Figure 17: (a) A one-square-angstrom STM image of freestanding graphene, acquired in the same manner as that in Fig. 14(a), but at a current of 4.00 nA and voltage of 0.1 V. Scale bar, 0.02 nm. (b) Height profile extracted from the STM image and showing a jump of nearly 60 nm at $t = 100$ s, mimicking a critical transition. Corresponding data from a gold sample is provided for comparison. The error bars represent the standard deviation of the 400 data points in the fast scan direction both before and after the large jump. (c) The measured tunneling current, which shows a large but unsaturated spike coinciding with the sudden displacement. (d) $A(t)$ for the graphene data. The variance, $A(0)$, is anomalously large when the mirror buckling effect occurs.

This unusual and unexpected event must be connected to heating the sample in the presence of an attractive force. We can interpret this effect as being due to mirror buckling of a thin shell. For example, for a spherical shell with radius R , the critical pressure p_c which causes mirror buckling is estimated as [126]

$$p_c \propto \sqrt{\frac{\kappa Y}{R^4}} \quad (18)$$

where $p_c \propto V_c^2$, and both κ and Y will be modified by the presence of heating and an electrostatic force. By increasing temperature (electric current), Y is reduced, and a lower bias voltage is required to invert the buckled structure. Also, a larger radius lowers the voltage that leads to a flip. At this specific current and voltage, a large buckled region below the tip is heated for 100 s and then suddenly changes its curvature from negative to positive, i.e., it switches from a bowl-like to a bump-like shape. This process is illustrated in Fig. 18. During Stage 1 [also labeled in Fig. 17(b)] the height increases as the tip begins to deform the bowl. A metastable state is reached at Stage 2 where the force is not large enough to keep altering the local graphene configuration. However, the critical pressure is finally reached as the temperature continues to rise, leading the system to suddenly switch to the more stable bump shape shown in Stage 3.

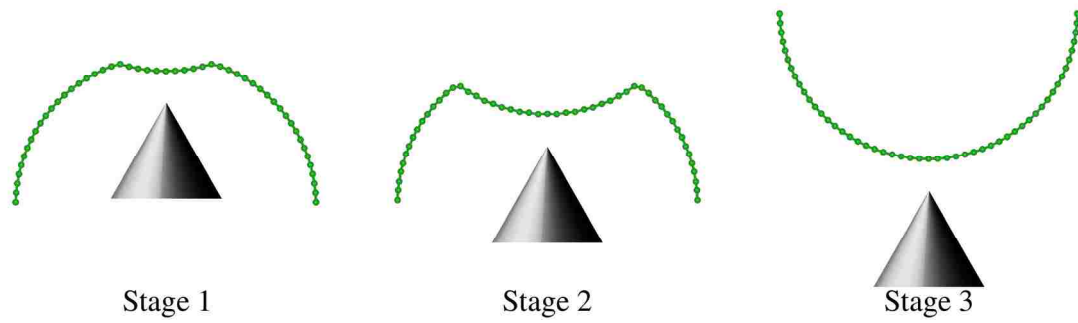


Figure 18: Series of illustrations depicting the stages of mirror buckling for a hemispherical shell. Corresponding labels are applied to the data in Fig. 17(b). A sudden inversion in the curvature occurs at the critical pressure, just before Stage 3.

V. SUMMARY

The STM is a versatile instrument that continues to break new ground. I have here demonstrated several of its capabilities on a flexible, conducting substrate. Specifically, I presented atomic-resolution STM images of graphene, including freestanding graphene. The graphene membrane was shown to be attracted to the STM tip, but the attractive force fluctuates periodically from a maximum over the carbon atoms to a minimum over the holes in the hexagonal structure. This gives rise to measuring an extremely large atomic corrugation in the images that must be interpreted as a combination of the electronic structure and elastic deformations working in tandem.

Constant-current STS is also a powerful tool to manipulate and study the atomic-scale properties of freestanding graphene. A series of feedback-on, tip-height measurements was collected at a single location on a sample of freestanding graphene by systematically changing the bias voltage and tunneling current. Increasing the bias voltage by 3 V resulted in the graphene being attracted to the STM tip and moving as much as 30 nm. On the other hand, increasing the setpoint current by 1 nA resulted in the graphene contracting away from the STM tip and moving as much as 20 nm, but in the opposite direction. A simple electrostatic model was used to quantify the attractive force between the tip and the sample, which was estimated to rise as high as 4 nN and explained the experimental dependence on bias voltage. From the induced strain, the magnitude of the pseudomagnetic field in the vicinity under the STM probe can be estimated.

The freestanding graphene was also modeled as an entropic rubber band to successfully account for its contraction as the current was increased, raising the temperature of the sample through Joule heating. The voltage and current data sets were shown to be consistent with each

other and to complement the understanding of one another. These results also highlight the very different interaction between a probe tip and flexible sample, compared to a stationary sample. Additionally, this technique allows one to locally quantify the unusual properties arising from graphene's negative thermal expansion coefficient.

Finally, the novel fluctuation measurements are a way to gain unprecedented insight into the dynamics of ripples in freestanding graphene using STM. While imaging an area the size of a single carbon atom, the vertical movement of the graphene is easily monitored with unparalleled precision. A degree of control over the shape and temperature of the membrane is applied through changing the tunneling parameters. The observed fluctuations are generally large and can be sorted based on exhibiting random, periodic, or mirror-buckling behavior. In particular, the periodic oscillations and their current-dependent characteristics were shown to be consistent with the predictions of elasticity theory under the influence of thermal stress. No other technique has demonstrated the ability to probe such low-frequency flexural phonon modes at the atomic scale, permitting direct investigation of the dynamic ripples that affect almost every property of graphene.

References

- [1] K.S. Novoselov, A.K. Geim, S.V. Morozov, D. Jiang, Y. Zhang, S.V. Dubonos, I.V. Grigorieva, A.A. Firsov, Electric field effect in atomically thin carbon films, *Science*, 306 (2004) 666-669.
- [2] A.K. Geim, K.S. Novoselov, The rise of graphene, *Nature Mater.*, 6 (2007) 183-191.
- [3] N.D. Mermin, Crystalline order in two dimensions, *Phys. Rev.*, 176 (1968) 250-254.
- [4] H. Shioyama, Cleavage of graphite to graphene, *J. Mater. Sci. Lett.*, 20 (2001) 499-500.
- [5] J.A. Venables, G.D.T. Spiller, M. Hanbücken, Nucleation and growth of thin films, *Rep. Prog. Phys.*, 47 (1984) 399-459.
- [6] L.M. Viculis, J.J. Mack, R.B. Kaner, A chemical route to carbon nanoscrolls, *Science*, 299 (2003) 1361.
- [7] P.R. Wallace, The band theory of graphite, *Phys. Rev.*, 71 (1947) 622-634.
- [8] A.H. Castro Neto, F. Guinea, N.M.R. Peres, K.S. Novoselov, A.K. Geim, The electronic properties of graphene, *Rev. Mod. Phys.*, 81 (2009) 109-162.
- [9] K.S. Novoselov, A.K. Geim, S.V. Morozov, D. Jiang, M.I. Katsnelson, I.V. Grigorieva, S.V. Dubonos, A.A. Firsov, Two-dimensional gas of massless Dirac fermions in graphene, *Nature*, 438 (2005) 197-200.
- [10] M.I. Katsnelson, K.S. Novoselov, A.K. Geim, Chiral tunnelling and the Klein paradox in graphene, *Nature Phys.*, 2 (2006) 620-625.
- [11] Y. Zhang, Y.-W. Tan, H.L. Stormer, P. Kim, Experimental observation of the quantum Hall effect and Berry's phase in graphene, *Nature*, 438 (2005) 201-204.
- [12] A.S. Mayorov, R.V. Gorbachev, S.V. Morozov, L. Britnell, R. Jalil, L.A. Ponomarenko, P. Blake, K.S. Novoselov, K. Watanabe, T. Taniguchi, A.K. Geim, Micrometer-scale ballistic transport in encapsulated graphene at room temperature, *Nano Lett.*, 11 (2011) 2396-2399.
- [13] C. Lee, X. Wei, J.W. Kysar, J. Hone, Measurement of the elastic properties and intrinsic strength of monolayer graphene, *Science*, 321 (2008) 385-388.
- [14] J.S. Bunch, S.S. Verbridge, J.S. Alden, A.M. van der Zande, J.M. Parpia, H.G. Craighead, P.L. McEuen, Impermeable atomic membranes from graphene sheets, *Nano Lett.*, 8 (2008) 2458-2462.
- [15] J.S. Bunch, A.M. van der Zande, S.S. Verbridge, I.W. Frank, D.M. Tanenbaum, J.M. Parpia, H.G. Craighead, P.L. McEuen, Electromechanical resonators from graphene sheets, *Science*, 315 (2007) 490-493.

- [16] J.C. Meyer, A.K. Geim, M.I. Katsnelson, K.S. Novoselov, D. Obergfell, S. Roth, C. Girit, A. Zettl, On the roughness of single- and bi-layer graphene membranes, *Solid State Commun.*, 143 (2007) 101-109.
- [17] J.C. Meyer, A.K. Geim, M.I. Katsnelson, K.S. Novoselov, T.J. Booth, S. Roth, The structure of suspended graphene sheets, *Nature*, 446 (2007) 60-63.
- [18] U. Bangert, M.H. Gass, A.L. Bleloch, R.R. Nair, J. Eccles, Nanotopography of graphene, *Phys. Status Solidi A*, 206 (2009) 2115-2119.
- [19] A. Fasolino, J.H. Los, M.I. Katsnelson, Intrinsic ripples in graphene, *Nature Mater.*, 6 (2007) 858-861.
- [20] K.S. Novoselov, D. Jiang, F. Schedin, T.J. Booth, V.V. Khotkevich, S.V. Morozov, A.K. Geim, Two-dimensional atomic crystals, *Proc. Natl. Acad. Sci. USA*, 102 (2005) 10451-10453.
- [21] X. Du, I. Skachko, F. Duerr, A. Luican, E.Y. Andrei, Fractional quantum Hall effect and insulating phase of Dirac electrons in graphene, *Nature*, 462 (2009) 192-195.
- [22] P. Blake, E.W. Hill, A.H. Castro Neto, K.S. Novoselov, D. Jiang, R. Yang, T.J. Booth, A.K. Geim, Making graphene visible, *Appl. Phys. Lett.*, 91 (2007) 063124.
- [23] C. Berger, Z. Song, T. Li, X. Li, A.Y. Ogbazghi, R. Feng, Z. Dai, A.N. Marchenkov, E.H. Conrad, P.N. First, W.A. de Heer, Ultrathin epitaxial graphite: 2D electron gas properties and a route toward graphene-based nanoelectronics, *J. Phys. Chem. B*, 108 (2004) 19912-19916.
- [24] C. Berger, Z. Song, X. Li, X. Wu, N. Brown, C. Naud, D. Mayou, T. Li, J. Hass, A.N. Marchenkov, E.H. Conrad, P.N. First, W.A. de Heer, Electronic confinement and coherence in patterned epitaxial graphene, *Science*, 312 (2006) 1191-1196.
- [25] L.O. Nyakiti, V.D. Wheeler, N.Y. Garces, R.L. Myers-Ward, C.R. Eddy, Jr., D.K. Gaskill, Enabling graphene-based technologies: toward wafer-scale production of epitaxial graphene, *MRS Bull.*, 37 (2012) 1149-1157.
- [26] C. Riedl, C. Coletti, U. Starke, Structural and electronic properties of epitaxial graphene on SiC(0001): a review of growth, characterization, transfer doping and hydrogen intercalation, *J. Phys. D: Appl. Phys.*, 43 (2010) 374009.
- [27] A. Reina, X. Jia, J. Ho, D. Nezich, H. Son, V. Bulovic, M.S. Dresselhaus, J. Kong, Large area, few-layer graphene films on arbitrary substrates by chemical vapor deposition, *Nano Lett.*, 9 (2009) 30-35.
- [28] J. Coraux, A.T. N'Diaye, C. Busse, T. Michely, Structural coherency of graphene on Ir(111), *Nano Lett.*, 8 (2008) 565-570.
- [29] S. Marchini, S. Günther, J. Wintterlin, Scanning tunneling microscopy of graphene on Ru(0001), *Phys. Rev. B*, 76 (2007) 075429.

- [30] X. Li, W. Cai, J. An, S. Kim, J. Nah, D. Yang, R. Piner, A. Velamakanni, I. Jung, E. Tutuc, S.K. Banerjee, L. Colombo, R.S. Ruoff, Large-area synthesis of high-quality and uniform graphene films on copper foils, *Science*, 324 (2009) 1312-1314.
- [31] H.I. Rasool, E.B. Song, M.J. Allen, J.K. Wassei, R.B. Kaner, K.L. Wang, B.H. Weiller, J.K. Gimzewski, Continuity of graphene on polycrystalline copper, *Nano Lett.*, 11 (2011) 251-256.
- [32] S. Bae, H. Kim, Y. Lee, X. Xu, J.-S. Park, Y. Zheng, J. Balakrishnan, T. Lei, H.R. Kim, Y.I. Song, Y.-J. Kim, K.S. Kim, B. Özyilmaz, J.-H. Ahn, B.H. Hong, S. Iijima, Roll-to-roll production of 30-inch graphene films for transparent electrodes, *Nature Nanotech.*, 5 (2010) 574-578.
- [33] X. Du, I. Skachko, A. Barker, E.Y. Andrei, Approaching ballistic transport in suspended graphene, *Nature Nanotech.*, 3 (2008) 491-495.
- [34] S. Das Sarma, S. Adam, E.H. Hwang, E. Rossi, Electronic transport in two-dimensional graphene, *Rev. Mod. Phys.*, 83 (2011) 407-470.
- [35] J.-H. Chen, C. Jang, S. Xiao, M. Ishigami, M.S. Fuhrer, Intrinsic and extrinsic performance limits of graphene devices on SiO₂, *Nature Nanotech.*, 3 (2008) 206-209.
- [36] S. Fratini, F. Guinea, Substrate-limited electron dynamics in graphene, *Phys. Rev. B*, 77 (2008) 195415.
- [37] K.I. Bolotin, K.J. Sikes, Z. Jiang, M. Klima, G. Fudenberg, J. Hone, P. Kim, H.L. Stormer, Ultrahigh electron mobility in suspended graphene, *Solid State Commun.*, 146 (2008) 351-355.
- [38] K.I. Bolotin, K.J. Sikes, J. Hone, H.L. Stormer, P. Kim, Temperature-dependent transport in suspended graphene, *Phys. Rev. Lett.*, 101 (2008) 096802.
- [39] W. Bao, F. Miao, Z. Chen, H. Zhang, W. Jang, C. Dames, C.N. Lau, Controlled ripple texturing of suspended graphene and ultrathin graphite membranes, *Nature Nanotech.*, 4 (2009) 562-566.
- [40] A.A. Balandin, S. Ghosh, W. Bao, I. Calizo, D. Teweldebrhan, F. Miao, C.N. Lau, Superior thermal conductivity of single-layer graphene, *Nano Lett.*, 8 (2008) 902-907.
- [41] M.H. Gass, U. Bangert, A.L. Bleloch, P. Wang, R.R. Nair, A.K. Geim, Free-standing graphene at atomic resolution, *Nature Nanotech.*, 3 (2008) 676-681.
- [42] I.W. Frank, D.M. Tanenbaum, A.M. van der Zande, P.L. McEuen, Mechanical properties of suspended graphene sheets, *J. Vac. Sci. Technol. B*, 25 (2007) 2558-2561.
- [43] M. Poot, H.S.J. van der Zant, Nanomechanical properties of few-layer graphene membranes, *Appl. Phys. Lett.*, 92 (2008) 063111.
- [44] A.K. Geim, Graphene: status and prospects, *Science*, 324 (2009) 1530-1534.

- [45] K.S. Novoselov, V.I. Fal'ko, L. Colombo, P.R. Gellert, M.G. Schwab, K. Kim, A roadmap for graphene, *Nature*, 490 (2012) 192-200.
- [46] G. Binnig, H. Rohrer, Scanning tunneling microscopy—from birth to adolescence, *Rev. Mod. Phys.*, 59 (1987) 615-625.
- [47] G. Binnig, H. Rohrer, C. Gerber, E. Weibel, Tunneling through a controllable vacuum gap, *Appl. Phys. Lett.*, 40 (1982) 178-180.
- [48] G. Binnig, H. Rohrer, C. Gerber, E. Weibel, 7×7 reconstruction on Si(111) resolved in real space, *Phys. Rev. Lett.*, 50 (1983) 120-123.
- [49] G. Binnig, H. Rohrer, Scanning tunneling microscopy, *Surf. Sci.*, 126 (1983) 236-244.
- [50] R.M. Feenstra, J.A. Stroscio, J. Tersoff, A.P. Fein, Atom-selective imaging of the GaAs(110) surface, *Phys. Rev. Lett.*, 58 (1987) 1192-1195.
- [51] V.P. LaBella, H. Yang, D.W. Bullock, P.M. Thibado, P. Kratzer, M. Scheffler, Atomic structure of the GaAs(001)-(2x4) surface resolved using scanning tunneling microscopy and first-principles theory, *Phys. Rev. Lett.*, 83 (1999) 2989-2992.
- [52] R.M. Feenstra, J.A. Stroscio, A.P. Fein, Tunneling spectroscopy of the Si(111) 2x1 surface, *Surf. Sci.*, 181 (1987) 295-306.
- [53] D.M. Eigler, E.K. Schweizer, Positioning single atoms with a scanning tunnelling microscope, *Nature*, 344 (1990) 524-526.
- [54] J.A. Stroscio, D.M. Eigler, Atomic and molecular manipulation with the scanning tunneling microscope, *Science*, 254 (1991) 1319-1326.
- [55] M.F. Crommie, C.P. Lutz, D.M. Eigler, Confinement of electrons to quantum corrals on a metal surface, *Science*, 262 (1993) 218-220.
- [56] R. Wiesendanger, *Scanning Probe Microscopy and Spectroscopy: Methods and Applications*, Cambridge University Press, Cambridge, UK, 1994.
- [57] J. Tersoff, D.R. Hamann, Theory and application for the scanning tunneling microscope, *Phys. Rev. Lett.*, 50 (1983) 1998-2001.
- [58] J. Tersoff, D.R. Hamann, Theory of the scanning tunneling microscope, *Phys. Rev. B*, 31 (1985) 805-813.
- [59] J.A. Stroscio, R.M. Feenstra, A.P. Fein, Electronic structure of the Si(111) 2x1 surface by scanning-tunneling microscopy, *Phys. Rev. Lett.*, 57 (1986) 2579-2582.
- [60] N.D. Lang, Spectroscopy of single atoms in the scanning tunneling microscope, *Phys. Rev. B*, 34 (1986) 5947-5950.

- [61] N.D. Lang, Apparent barrier height in scanning tunneling microscopy, *Phys. Rev. B*, 37 (1988) 10395-10398.
- [62] J.F. Xu, P.M. Thibado, Z. Ding, 4 K, ultrahigh vacuum scanning tunneling microscope having two orthogonal tips with tunnel junctions as close as a few nanometers, *Rev. Sci. Instrum.*, 77 (2006) 093703.
- [63] J.K. Schoelz, P. Xu, S.D. Barber, D. Qi, M.L. Ackerman, G. Basnet, C.T. Cook, P.M. Thibado, High-percentage success method for preparing and pre-evaluating tungsten tips for atomic-resolution scanning tunneling microscopy, *J. Vac. Sci. Technol. B*, 30 (2012) 033201.
- [64] G. Basnet, J.K. Schoelz, P. Xu, S.D. Barber, M.L. Ackerman, P.M. Thibado, Etch-stop method for reliably fabricating sharp yet mechanically stable scanning tunneling microscope tips, *J. Vac. Sci. Technol. B*, 31 (2013) 043201.
- [65] L.A. Hockett, S.E. Creager, A convenient method for removing surface oxides from tungsten STM tips, *Rev. Sci. Instrum.*, 64 (1993) 263-264.
- [66] A. Luican, G. Li, A. Reina, J. Kong, R.R. Nair, K.S. Novoselov, A.K. Geim, E.Y. Andrei, Single-layer behavior and its breakdown in twisted graphene layers, *Phys. Rev. Lett.*, 106 (2011) 126802.
- [67] D. Tománek, S.G. Louie, H.J. Mamin, D.W. Abraham, R.E. Thomson, E. Ganz, J. Clarke, Theory and observation of highly asymmetric atomic structure in scanning-tunneling-microscopy images of graphite, *Phys. Rev. B*, 35 (1987) 7790-7793.
- [68] D. Tománek, S.G. Louie, First-principles calculation of highly asymmetric structure in scanning-tunneling-microscopy images of graphite, *Phys. Rev. B*, 37 (1988) 8327-8336.
- [69] P. Xu, Y. Yang, S.D. Barber, M.L. Ackerman, J.K. Schoelz, I.A. Kornev, S. Barraza-Lopez, L. Bellaiche, P.M. Thibado, Giant surface charge density of graphene resolved from scanning tunneling microscopy and first-principles theory, *Phys. Rev. B*, 84 (2011) 161409(R).
- [70] J.M. Soler, A.M. Baro, N. García, H. Rohrer, Interatomic forces in scanning tunneling microscopy: giant corrugations of the graphite surface, *Phys. Rev. Lett.*, 57 (1986) 444-447.
- [71] P. Xu, Y. Yang, S.D. Barber, M.L. Ackerman, J.K. Schoelz, D. Qi, I.A. Kornev, L. Dong, L. Bellaiche, S. Barraza-Lopez, P.M. Thibado, Atomic control of strain in freestanding graphene, *Phys. Rev. B*, 85 (2012) 121406(R).
- [72] R.S. Becker, J.A. Golovchenko, B.S. Swartzentruber, Electron interferometry at crystal surfaces, *Phys. Rev. Lett.*, 55 (1985) 987-990.
- [73] G. Binnig, K.H. Frank, H. Fuchs, N. Garcia, B. Reihl, H. Rohrer, F. Salvan, A.R. Williams, Tunneling spectroscopy and inverse photoemission: image and field states, *Phys. Rev. Lett.*, 55 (1985) 991-994.

- [74] V.M. Pereira, A.H. Castro Neto, H.Y. Liang, L. Mahadevan, Geometry, mechanics, and electronics of singular structures and wrinkles in graphene, *Phys. Rev. Lett.*, 105 (2010) 156603.
- [75] L. Dong, J. Hansen, P. Xu, M.L. Ackerman, S.D. Barber, J.K. Schoelz, D. Qi, P.M. Thibado, Electromechanical properties of freestanding graphene functionalized with tin oxide (SnO₂) nanoparticles, *Appl. Phys. Lett.*, 101 (2012) 061601.
- [76] P. Xu, L. Dong, M. Neek-Amal, M.L. Ackerman, J. Yu, S.D. Barber, J.K. Schoelz, D. Qi, F. Xu, P.M. Thibado, F.M. Peeters, Self-organized platinum nanoparticles on freestanding graphene, *ACS Nano*, 8 (2014) 2697-2703.
- [77] V.M. Pereira, A.H. Castro Neto, Strain engineering of graphene's electronic structure, *Phys. Rev. Lett.*, 103 (2009) 046801.
- [78] F. Guinea, Strain engineering in graphene, *Solid State Commun.*, 152 (2012) 1437-1441.
- [79] N.N. Klimov, S. Jung, S. Zhu, T. Li, C.A. Wright, S.D. Solares, D.B. Newell, N.B. Zhitenev, J.A. Stroschio, Electromechanical properties of graphene drumheads, *Science*, 336 (2012) 1557-1561.
- [80] T. Mashoff, M. Pratzner, V. Geringer, T.J. Echtermeyer, M.C. Lemme, M. Liebmann, M. Morgenstern, Bistability and oscillatory motion of natural nanomembranes appearing within monolayer graphene on silicon dioxide, *Nano Lett.*, 10 (2010) 461-465.
- [81] F.R. Eder, J. Kotakoski, K. Holzweber, C. Mangler, V. Skakalova, J.C. Meyer, Probing from both sides: reshaping the graphene landscape via face-to-face dual-probe microscopy, *Nano Lett.*, 13 (2013) 1934-1940.
- [82] W.R. Smythe, *Static and Dynamic Electricity*, 1 ed., McGraw-Hill, New York, 1939.
- [83] F.F. Dall'Agnol, V.P. Mammana, Solution for the electric potential distribution produced by sphere-plane electrodes using the method of images, *Rev. Bras. Ensino Fis.*, 31 (2009) 3503.
- [84] P. Xu, S.D. Barber, M.L. Ackerman, J.K. Schoelz, P.M. Thibado, Role of bias voltage and tunneling current in the perpendicular displacements of freestanding graphene via scanning tunneling microscopy, *J. Vac. Sci. Technol. B*, 31 (2013) 04D103.
- [85] A. Sadeghi, A. Baratoff, S.A. Ghasemi, S. Goedecker, T. Glatzel, S. Kawai, E. Meyer, Multiscale approach for simulations of Kelvin probe force microscopy with atomic resolution, *Phys. Rev. B*, 86 (2012) 075407.
- [86] B.-F. Ju, Y.-L. Chen, Y. Ge, The art of electrochemical etching for preparing tungsten probes with controllable tip profile and characteristic parameters, *Rev. Sci. Instrum.*, 82 (2011) 013707.
- [87] M.A.H. Vozmediano, M.I. Katsnelson, F. Guinea, Gauge fields in graphene, *Phys. Rep.*, 496 (2010) 109-148.

- [88] C.L. Kane, E.J. Mele, Size, shape, and low energy electronic structure of carbon nanotubes, *Phys. Rev. Lett.*, 78 (1997) 1932-1935.
- [89] F. Guinea, M.I. Katsnelson, A.K. Geim, Energy gaps and a zero-field quantum Hall effect in graphene by strain engineering, *Nature Phys.*, 6 (2010) 30-33.
- [90] N. Levy, S.A. Burke, K.L. Meaker, M. Panlasigui, A. Zettl, F. Guinea, A.H. Castro Neto, M.F. Crommie, Strain-induced pseudo-magnetic fields greater than 300 tesla in graphene nanobubbles, *Science*, 329 (2010) 544-547.
- [91] W.H. Duan, C.M. Wang, Nonlinear bending and stretching of a circular graphene sheet under a central point load, *Nanotechnology*, 20 (2009) 075702.
- [92] M. Abramowitz, I.A. Stegun, Handbook of Mathematical Functions with Formulas, Graphs, and Mathematical Tables, in: National Bureau of Standards Applied Mathematics Series, U.S. Department of Commerce, Washington, DC, 1972.
- [93] S. Barraza-Lopez, A.A. Pacheco Sanjuan, Z. Wang, M. Vanević, Strain-engineering of graphene's electronic structure beyond continuum elasticity, *Solid State Commun.*, 166 (2013) 70-75.
- [94] J.V. Sloan, A.A. Pacheco Sanjuan, Z. Wang, C. Horvath, S. Barraza-Lopez, Strain gauge fields for rippled graphene membranes under central mechanical load: an approach beyond first-order continuum elasticity, *Phys. Rev. B*, 87 (2013) 155436.
- [95] N. Lindahl, D. Midtvedt, J. Svensson, O.A. Nerushev, N. Lindvall, A. Isacson, E.E.B. Campbell, Determination of the bending rigidity of graphene via electrostatic actuation of buckled membranes, *Nano Lett.*, 12 (2012) 3526-3531.
- [96] S. Scharfenberg, D.Z. Rocklin, C. Chialvo, R.L. Weaver, P.M. Goldbart, N. Mason, Probing the mechanical properties of graphene using a corrugated elastic substrate, *Appl. Phys. Lett.*, 98 (2011) 091908.
- [97] K.N. Kudin, G.E. Scuseria, B.I. Yakobson, C₂F, BN, and C nanoshell elasticity from *ab initio* computations, *Phys. Rev. B*, 64 (2001) 235406.
- [98] Q. Lu, M. Arroyo, R. Huang, Elastic bending modulus of monolayer graphene, *J. Phys. D: Appl. Phys.*, 42 (2009) 102002.
- [99] H. Suzuura, T. Ando, Phonons and electron-phonon scattering in carbon nanotubes, *Phys. Rev. B*, 65 (2002) 235412.
- [100] F. Flores, P.M. Echenique, R.H. Ritchie, Energy dissipation processes in scanning tunneling microscopy, *Phys. Rev. B*, 34 (1986) 2899-2902.
- [101] M. Pozzo, D. Alfè, P. Lacovig, P. Hofmann, S. Lizzit, A. Baraldi, Thermal expansion of supported and freestanding graphene: lattice constant versus interatomic distance, *Phys. Rev. Lett.*, 106 (2011) 135501.

- [102] N. Mounet, N. Marzari, First-principles determination of the structural, vibrational and thermodynamic properties of diamond, graphite, and derivatives, *Phys. Rev. B*, 71 (2005) 205214.
- [103] K.V. Zakharchenko, M.I. Katsnelson, A. Fasolino, Finite temperature lattice properties of graphene beyond the quasiharmonic approximation, *Phys. Rev. Lett.*, 102 (2009) 046808.
- [104] G. Savarino, M.R. Fisch, A general physics laboratory investigation of the thermodynamics of a rubber band, *Am. J. Phys.*, 59 (1991) 141-145.
- [105] A.C. Tribble, *Princeton Guide to Advanced Physics*, Princeton University Press, Princeton, NJ, 1996.
- [106] G. Ehrlich, F.G. Hudda, Atomic view of surface self-diffusion: tungsten on tungsten, *J. Chem. Phys.*, 44 (1966) 1039-1049.
- [107] Y.W. Mo, J. Kleiner, M.B. Webb, M.G. Lagally, Activation energy for surface diffusion of Si on Si(001): a scanning-tunneling-microscopy study, *Phys. Rev. Lett.*, 66 (1991) 1998-2001.
- [108] B.S. Swartzentruber, Direct measurement of surface diffusion using atom-tracking scanning tunneling microscopy, *Phys. Rev. Lett.*, 76 (1996) 459-462.
- [109] A. Smolyanitsky, V.K. Tewary, Manipulation of graphene's dynamic ripples by local harmonic out-of-plane excitation, *Nanotechnology*, 24 (2013) 055701.
- [110] P.L. de Andres, F. Guinea, M.I. Katsnelson, Bending modes, anharmonic effects, and thermal expansion coefficient in single-layer and multilayer graphene, *Phys. Rev. B*, 86 (2012) 144103.
- [111] L. Lindsay, D.A. Broido, N. Mingo, Flexural phonons and thermal transport in graphene, *Phys. Rev. B*, 82 (2010) 115427.
- [112] E.V. Castro, H. Ochoa, M.I. Katsnelson, R.V. Gorbachev, D.C. Elias, K.S. Novoselov, A.K. Geim, F. Guinea, Limits on charge carrier mobility in suspended graphene due to flexural phonons, *Phys. Rev. Lett.*, 105 (2010) 266601.
- [113] P. Partovi-Azar, N. Nafari, M.R.R. Tabar, Interplay between geometrical structure and electronic properties in rippled free-standing graphene, *Phys. Rev. B*, 83 (2011) 165434.
- [114] J.H. Los, M.I. Katsnelson, O.V. Yazyev, K.V. Zakharchenko, A. Fasolino, Scaling properties of flexible membranes from atomistic simulations: application to graphene, *Phys. Rev. B*, 80 (2009) 121405(R).
- [115] U.M.B. Marconi, A. Puglisi, L. Rondoni, A. Vulpiani, Fluctuation-dissipation: response theory in statistical physics, *Phys. Rep.*, 461 (2008) 111-195.
- [116] A. Savitzky, M.J.E. Golay, Smoothing and differentiation of data by simplified least squares procedures, *Anal. Chem.*, 36 (1964) 1627-1639.

- [117] J. Steinier, Y. Termonia, J. Deltour, Comments on smoothing and differentiation of data by simplified least square procedure, *Anal. Chem.*, 44 (1972) 1906-1909.
- [118] J.H. Seol, I. Jo, A.L. Moore, L. Lindsay, Z.H. Aitken, M.T. Pettes, X. Li, Z. Yao, R. Huang, D. Broido, N. Mingo, R.S. Ruoff, L. Shi, Two-dimensional phonon transport in supported graphene, *Science*, 328 (2010) 213-216.
- [119] E. Mariani, F. von Oppen, Flexural phonons in free-standing graphene, *Phys. Rev. Lett.*, 100 (2008) 076801.
- [120] N. Bonini, M. Lazzeri, N. Marzari, F. Mauri, Phonon anharmonicities in graphite and graphene, *Phys. Rev. Lett.*, 99 (2007) 176802.
- [121] R. Zan, C. Muryn, U. Bangert, P. Mattocks, P. Wincott, D. Vaughan, X. Li, L. Colombo, R.S. Ruoff, B. Hamilton, K.S. Novoselov, Scanning tunnelling microscopy of suspended graphene, *Nanoscale*, 4 (2012) 3065-3068.
- [122] C. Chen, Graphene NanoElectroMechanical Resonators and Oscillators, Ph.D. Thesis, Columbia University, New York, NY, 2013.
- [123] L.D. Landau, E.M. Lifshitz, *Theory of Elasticity*, 2 ed., Pergamon Press, Oxford, 1970.
- [124] P. Xu, M. Neek-Amal, S.D. Barber, M.L. Ackerman, J.K. Schoelz, P.M. Thibado, A. Sadeghi, F.M. Peeters, Unusual ultra-low frequency fluctuations in freestanding graphene, *Nat. Commun.*, Article in press. (2014).
- [125] P.L. de Andres, F. Guinea, M.I. Katsnelson, Density functional theory analysis of flexural modes, elastic constants, and corrugations in strained graphene, *Phys. Rev. B*, 86 (2012) 245409.
- [126] A.V. Pogorelov, *Bendings of Surfaces and Stability of Shells*, American Mathematical Society, Providence, RI, 1988.

Appendix A: Bessel Function Ratio

```
function [ q ] = dividelargebesseli( n1,arg1,n2,arg2 )
```

```
% This is a MATLAB function to find the ratio between two modified Bessel functions of the  
% first kind which have real arguments that are too large to evaluate with the besseli(nu,Z)  
% function. It is currently optimized for application in solving Equation (7).
```

```
%
```

```
% Inputs:
```

```
% n1 - A scalar, the order of the Bessel function in the numerator.
```

```
% arg1 - A vector, the list of arguments for the Bessel function in the numerator.
```

```
% n2 - A scalar, the order of the Bessel function in the denominator.
```

```
% arg2 - A scalar, the argument for the Bessel function in the numerator. This could easily be  
% changed to be a vector, but in Eq. (7) it will be a scalar.
```

```
%
```

```
% Output:
```

```
% q - A vector, the list of final calculated ratios, one for each element of arg1.
```

```
% Determine how many elements are in the arg1 vector. Initialize the q vector to this size and fill  
% it with zeros.
```

```
s = size(arg1,2);
```

```
q = zeros([1 s]);
```

```

% This loop will calculate the ratio for each element individually. Since it will be zero when arg1
% is much less than arg2, the if-statement checks for this condition before proceeding.

for m = 1:s
if arg1(m) >= 0.9*arg2(1)

% This section computes the part in brackets in Eq. (8) for the Bessel function in the numerator
% (num) and denominator (den), then finds their ratio (f).

num = 1-(4*n1^2-1)/(8*arg1(m))+(4*n1^2-1)*(4*n1^2-9)/(2*(8*arg1(m))^2)-(4*n1^2-
    1)*(4*n1^2-9)*(4*n1^2-25)/(6*(8*arg1(m))^3);
den = 1-(4*n2^2-1)/(8*arg2(1))+(4*n2^2-1)*(4*n2^2-9)/(2*(8*arg2(1))^2)-(4*n2^2-
    1)*(4*n2^2-9)*(4*n2^2-25)/(6*(8*arg2(1))^3);

f = num/den;

% Finally, f is combined with the exponential factor at the beginning of Eq. (8) to get the final
% ratio (q).

q(m) = f*sqrt(arg2(1)/arg1(m))*exp(arg1(m)-arg2(1));

end

end

end

```

Appendix B: Graphene Height under Central Load

```
function [ r,w ] = deflection( a,F )
```

```
% This is a MATLAB function to evaluate Eq. (7) for the vertical deflection of a circular  
% graphene membrane under a central point load. It requires the use of dividelargebesseli found  
% in Appendix A.
```

```
%
```

```
% Inputs:
```

```
% a - A scalar, the radius of the circular graphene sheet, in nanometers.
```

```
% F - A scalar, the force applied by the central point load, in nanonewtons.
```

```
%
```

```
% Outputs:
```

```
% r - A vector, all the radial positions at which the deflection was computed, in nanometers.
```

```
% w - A vector, the vertical deflection of the graphene at each position (r), in nanometers.
```

```
% The force is converted from nN to eV/nm. Then the flexural rigidity (D) is set, in eV. To
```

```
% change the initial in-plane tension, adjust the "1.2" (eV/nm2) in the formula for "lam". P and
```

```
% lam are dimensionless quantities used later.
```

```
F = F*6.24150932378;
```

```
D = 7.1;
```

```
P = F*a/D;
```

```
lam = sqrt(1.2*a2/D);
```

% Eta is the dimensionless radial variable. This creates an eta vector with 10,000 elements

% evenly spaced from just over 0 to 1. The deflection will be calculated at each of these

% locations. You can choose any range between 0 and 1, but it will not work at eta = 0.

```
eta = linspace(0.005/a,1,10000);
```

% Eq. (7) is evaluated here, adding an element to the dimensionless height vector W for each one

% in eta.

```
W = (P/(2*pi*lam^2))*((dividelargebesseli(0, lam*eta, 1, lam)-
```

```
dividelargebesseli(0, lam, 1, lam))*(1-lam*besselk(1, lam))/lam+besselk(0, lam)-
```

```
besselk(0, lam*eta)-log(eta));
```

% Get the position and height in nm.

```
r = a*eta;
```

```
w = a*W;
```

% Switch r and w from rows to columns for convenience.

```
r = transpose(r);
```

```
w = transpose(w);
```

```
end
```

Appendix C: Pseudomagnetic Field Calculation

```
function [ B ] = magfield( r,u )
```

```
% This is a MATLAB function to numerically evaluate B(r) in Eq. (10), the radially dependent  
% part of the pseudomagnetic field for a circular graphene sample under a known circularly  
% symmetric strain.
```

```
%
```

```
% Inputs:
```

```
% r - A vector, all the radial positions (in nm) at which B should be calculated. The elements of r  
% must be evenly spaced.
```

```
% u - A vector the same size as r, the radial strain (in nm) at each location r. The elements of u  
% should change slowly with respect to the step size of r.
```

```
%
```

```
% Output:
```

```
% B - A vector, the pseudomagnetic field (in teslas) at each value of r, given in the same order.
```

```
% Set beta and the lattice constant a (in nm).
```

```
bet = 2;
```

```
a = 0.246;
```

```
% Determine the step size in the vector r.
```

```
h = r(2)-r(1);
```

```
% Calculate the first (v) and second (w) derivatives of u with respect to r.
```

```
v = gradient(u,h);
```

```
w = gradient(v,h);
```

```
% Compute B and convert it to teslas.
```

```
B = (bet/a).*(w-(3./r).*v+3.*u./r.^2).*658.265;
```

```
end
```

Appendix D: The Rubber Band Problem

A rubber band is fastened at one end to a peg and supports from its other end a weight F . Assume a simple microscopic model for the rubber band which consists of a linked polymer chain of N segments [$N = O(10^{23})$] joined end to end. Each segment has a length ℓ and can be oriented either parallel to the vertical direction. Neglect the kinetic energies or weights of the segments themselves, or any interaction between the segments. The rubber band is in equilibrium with its surroundings at temperature T . Compute the equilibrium length L .

Let the number of segments pointing down be n , so the number pointing up is $N - n$.

Then the length of the rubber band is

$$L = \ell[n - (N - n)] = \ell[2n - N]$$

and the energy of the configuration is

$$E = -F \times L = -F\ell[2n - N]$$

For use in a moment, solve this equation for n :

$$2n - N = \frac{-E}{F\ell} \Rightarrow n = \frac{1}{2} \left(N - \frac{E}{F\ell} \right)$$

Also note that

$$N - n = N - \frac{1}{2}N + \frac{1}{2} \frac{E}{F\ell} = \frac{1}{2}N + \frac{1}{2} \frac{E}{F\ell} = \frac{1}{2} \left(N + \frac{E}{F\ell} \right)$$

The entropy of the configuration is

$$S = k \ln \left[\frac{N!}{(N - n)! n!} \right] = k \{ \ln(N!) - \ln[(N - n)!] - \ln(n!) \}$$

where the argument of the first logarithm is the number of different ways to arrange the segments. Use Stirling's approximation [$\ln(m!) = m \ln m - m$, for large m] to simplify:

$$S = k \{ N \ln N - N - (N - n) \ln(N - n) + (N - n) - n \ln n + n \}$$

$$S = k\{N \ln N - (N - n) \ln(N - n) - n \ln n\}$$

Substitute into this the above expressions for n and $N - n$ to get $S(E)$:

$$S(E) = k \left\{ N \ln N - \left[\frac{1}{2} \left(N + \frac{E}{F\ell} \right) \right] \ln \left[\frac{1}{2} \left(N + \frac{E}{F\ell} \right) \right] - \left[\frac{1}{2} \left(N - \frac{E}{F\ell} \right) \right] \ln \left[\frac{1}{2} \left(N - \frac{E}{F\ell} \right) \right] \right\}$$

To relate this with the temperature, use the fact that $1/T = \partial S / \partial E$:

$$\frac{1}{T} = \frac{\partial S}{\partial E} = \frac{-k}{2F\ell} \left\{ \ln \left[\frac{1}{2} \left(N + \frac{E}{F\ell} \right) \right] - \ln \left[\frac{1}{2} \left(N - \frac{E}{F\ell} \right) \right] \right\} = \frac{k}{2F\ell} \ln \left[\frac{N - E/(F\ell)}{N + E/(F\ell)} \right]$$

Now rearrange and manipulate to isolate $E/(F\ell)$:

$$\ln \left[\frac{N - E/(F\ell)}{N + E/(F\ell)} \right] = \frac{2F\ell}{kT} \Rightarrow \frac{N - E/(F\ell)}{N + E/(F\ell)} = e^{2F\ell/(kT)}$$

$$N - \frac{E}{F\ell} = N e^{2F\ell/(kT)} + \frac{E}{F\ell} e^{2F\ell/(kT)} \Rightarrow \frac{E}{F\ell} e^{2F\ell/(kT)} + \frac{E}{F\ell} = N - N e^{2F\ell/(kT)}$$

$$\frac{E}{F\ell} [e^{2F\ell/(kT)} + 1] = -N [e^{2F\ell/(kT)} - 1] \Rightarrow \frac{E}{F\ell} = -N \frac{e^{2F\ell/(kT)} - 1}{e^{2F\ell/(kT)} + 1} = -N \tanh \left(\frac{F\ell}{kT} \right)$$

Since $L = -E/F$,

$$L = -\frac{E}{F} = N\ell \tanh \left(\frac{F\ell}{kT} \right)$$

The Taylor series expansion for hyperbolic tangent is

$$\tanh x = x - \frac{x^3}{3} + \frac{2x^5}{15} - \frac{17x^7}{315} + \dots$$

So to first order (for small forces and/or large temperatures):

$$L = \left(\frac{N\ell^2}{k} \right) \frac{F}{T}$$

Appendix E: Graphene Height as Function of Current

This is the development of Eq. (11), a fitting equation for the height of a freestanding graphene membrane under a STM tip when the graphene is being locally heated by an increasing tunneling current I . The total tip height Z is the sum of the local graphene height h and the tip-sample separation s . Each component will be considered separately, beginning with s .

We already know from STM tunneling theory that $I \propto e^{-2cs}$ [Eq. (1)], where c is related to the work function of the sample. This can be written as:

$$I = I_0 e^{-2cs}$$

Assuming the electrical resistance of graphene is negligible compared with the vacuum, and we apply a constant bias V_0 :

$$I = \frac{V_0}{R_0} e^{-2cs}$$

where R_0 is a constant, but the general vacuum resistance R varies with s . Next some simple algebra must be performed to arrive at s as a function of I .

$$e^{-2cs} = \frac{IR_0}{V_0} \Rightarrow -2cs = \ln\left(\frac{IR_0}{V_0}\right)$$

$$s = \frac{-1}{2c} \ln\left(\frac{IR_0}{V_0}\right) = \frac{1}{2c} \ln\left(\frac{V_0}{IR_0}\right)$$

s therefore increases logarithmically if V increases or I decreases while the other quantity is held constant. Separating the I dependence:

$$s = \frac{-1}{2c} \ln(I) + \frac{1}{2c} \ln\left(\frac{V_0}{R_0}\right) = b \ln(I) + d$$

where b and d are constants to be determined by fitting.

Next, we need an expression for h as a function of I . To first approximation, the change in height of graphene is related to temperature T by a linear thermal expansion coefficient α :

$$\frac{dh}{dT} = -\alpha h$$

Note that the coefficient should be negative for graphene. I choose to let α be positive and make the negative sign explicit. Then, assuming the temperature increase under the tip is proportional to I^2 (Joule heating):

$$T = \beta I^2 + T_0 \Rightarrow dT = 2\beta I dI$$

where β and T_0 are constants. Now substitute dT into the previous equation:

$$\frac{dh}{dT} = \frac{dh}{2\beta I dI} = -\alpha h \Rightarrow \frac{dh}{dI} = -2k h I$$

where I have combined constants to let $\beta\alpha = k$. This is solvable by separation of variables:

$$\frac{dh}{h} = -2k I dI$$

Letting h_0 be the height when $I = 0$:

$$\int_{h_0}^h \frac{dh}{h} = -2k \int_0^I I dI$$

$$\ln\left(\frac{h}{h_0}\right) = -k I^2$$

$$h = h_0 e^{-k I^2}$$

The above results for s and h can now be combined to arrive at Eq. (11). Note that the constant d has been absorbed into z_{offset} , which also accounts for the unknown STM starting height:

$$Z = h + s = h_0 e^{-k I^2} + b \ln(I) + z_{\text{offset}}$$

Appendix F: Autocovariance and Periodogram Definitions

Autocovariance

Covariance is a measure of how much two random variables change together. It can be positive or negative depending on whether they change together or in opposite directions. The magnitude is related to strength of their *linear* relationship. If x and y are independent, their covariance $\sigma(x, y)$ is zero, but the converse is not necessarily true. Definition of covariance:

$$\sigma(x, y) = \langle [x - \langle x \rangle][y - \langle y \rangle] \rangle = \langle xy \rangle - \langle x \rangle \langle y \rangle$$

where $\langle x \rangle$ is the average value of x . This includes the formula for variance: $\sigma(x, x) = \sigma^2(x)$.

Given a random process, the autocovariance $\sigma_{xx}(\tau)$ is the covariance of the variable against a time-shifted version of itself. Definition of autocovariance (τ is the time shift):

$$\sigma_{xx}(\tau) = \langle [x(0) - \langle x(0) \rangle][x(\tau) - \langle x(\tau) \rangle] \rangle = \langle x(0)x(\tau) \rangle - \langle x(0) \rangle \langle x(\tau) \rangle$$

Autocorrelation is an even function. The maximum is always at $\tau = 0$. The autocorrelation of a periodic function is periodic with the same period.

Periodogram

The power spectral density describes how the power of a signal is distributed over different frequencies. For convenience, “power” is often defined generally as the squared value of the signal. If the Fourier transform $\hat{x}_T(\omega)$ of a signal $x(t)$ is:

$$\hat{x}_T(\omega) = \frac{1}{\sqrt{T}} \int_0^T x(t) e^{-i\omega t} dt$$

then the power spectral density $S_{xx}(\omega)$ is given by:

$$S_{xx}(\omega) = \lim_{T \rightarrow \infty} \langle |\hat{x}_T(\omega)|^2 \rangle$$

Also, $S_{xx}(\omega)$ and $\sigma_{xx}(t)$ are a Fourier transform pair. That is, $S_{xx}(\omega) = \int_{-\infty}^{+\infty} \sigma_{xx}(\tau) e^{-i\omega\tau} d\tau$.

However, for a finite time series x_n with $1 \leq n \leq N$, and a sample interval Δt so that $T = N\Delta t$,

the true power spectral density must be approximated by the periodogram:

$$S_{xx}(\omega) = \frac{(\Delta t)^2}{T} \left| \sum_{n=1}^N x_n e^{-i\omega n} \right|^2$$

Appendix G: Savitzky-Golay Program

/* This is C++ code for an executable program that will perform basic Savitzky-Golay smoothing and derivatives. It can read an input data file and create an output file.

Input File:

It is important that the input file meet certain requirements. First, it must contain two columns of data. The first column is for the independent parameter (or x-values), such as time. These have to be in equally spaced steps or the S-G algorithm will not work. The second column should contain the measured parameter (or y-values), with the same number of entries as the first column. Example:

0.0 5.4

0.1 4.9

0.2 5.1

0.3 4.6

etc

You need a large number of data points (many rows in the input file) for S-G to be worthwhile.

The columns can be separated by spaces or tabs as long as they are separated and contain only numbers. Your file can have a header. The program will ask how many lines in the input file need to be skipped, so you just need to know that. However, it should not have any text at the bottom. The last line should be data or blank. Finally, the input file can have any name. The program will ask for it. As long as the file is in the same folder as the program, you need only the file name. Otherwise, you will have to specify the directory.

Output File:

You will get to name the output file. It will be placed in the same folder as the program unless you specify a directory in addition to the file name. It will be formatted like the input file above.

The x and y columns will be tab-separated, and there will be no header. The x-values should be the same as the input file, except there will be a few points missing at the beginning and end. The exact number depends on how many data points you instruct the program to consider at once as it works. If your input data is too short, the output file may be blank. */

```
#include <fstream>
```

```
#include <iostream>
```

```
#include <cctype>
```

```
#include <new>
```

```
#include <cmath>
```

```
#include <string>
```

```
using namespace std;
```

```
// This is the default string length. It is set high to be able to accept any possible user input.
```

```
const int SL=1000;
```

```
/* MatrixMult is a general matrix multiplication function. Its full capabilities are not necessary for S-G, but I had already written it. As input, it requires the "first" and "second" matrices to be multiplied, a matrix of the proper size (caller must ensure) into which it will put the "result", the number of rows (R1) and columns (C1) in the first matrix, and the number of columns (C2) in
```

the second matrix. R2 is not requested since it has to equal C1 (caller must ensure this).

MatrixMult is used by CalcFit, CalcDeriv1, and CalcDeriv2. */

```
void MatrixMult(double **first, double **second, double **result, int R1, int C1, int C2)
```

```
{
```

```
int i, j, cnt;
```

```
double sum;
```

```
for (i = 0; i < R1; i++)
```

```
for (j = 0; j < C2; j++)
```

```
{
```

```
sum = 0;
```

```
for (cnt = 0; cnt < C1; cnt++)
```

```
sum += first[i][cnt] * second[cnt][j];
```

```
result[i][j] = sum;
```

```
}
```

```
}
```

/* CalcFit, CalcDeriv1, and CalcDeriv2 are all called by main to perform the bulk of the S-G algorithm. CalcFit is for smoothing, CalcDeriv1 for taking the first derivative, and CalcDeriv2 for taking the second derivative. S-G is capable of higher order derivatives, and these could be added without great difficulty, but they are rarely needed and thus excluded. As input, they all

require a subset of the Y data ($2*m+1$ points), B for writing the result, the order (n) of polynomials used for fitting, and the number of data points ($2*m+1$) to consider at once. I will comment within CalcFit only since the other functions are very similar. */

```
void CalcFit(double **Y, double **B, int n, int m)
```

```
{
```

```
int i;
```

```
/* The QuadCub matrix contains the convoluting integers (first  $2*m+1$  in each row) and normalization factors (last entry in each row) for all m (2 through 12 from top to bottom) when n is 2 or 3 (quadratic or cubic fitting). There is no difference; if the user asks for quadratic fitting, they will actually get cubic. This is just a byproduct of the mathematical procedure. It is possible to calculate these numbers on the fly, but it was ultimately simpler to hard code them. */
```

```
double QuadCub[11][26]={
```

```
{-3,12,17,12,-3,35},
```

```
{-2,3,6,7,6,3,-2,21},
```

```
{-21,14,39,54,59,54,39,14,-21,231},
```

```
{-36,9,44,69,84,89,84,69,44,9,-36,429},
```

```
{-11,0,9,16,21,24,25,24,21,16,9,0,-11,143},
```

```
{-78,-13,42,87,122,147,162,167,162,147,122,87,42,-13,-78,1105},
```

```
{-21,-6,7,18,27,34,39,42,43,42,39,34,27,18,7,-6,-21,323},
```

```
{-136,-51,24,89,144,189,224,249,264,269,264,249,224,189,144,89,24,-51,-136,2261},
```

```
{-171,-76,9,84,149,204,249,284,309,324,329,324,309,284,249,204,149,84,9,-76,-171,3059},
```

```
{-42,-21,-2,15,30,43,54,63,70,75,78,79,78,75,70,63,54,43,30,15,-2,-21,-42,805},
```

```
{-253,-138,-33,62,147,222,287,342,387,422,447,462,467,462,447,422,387,342,287,222,147,62,  
-33,-138,-253,5175}
```

```
};
```

```
// Same as above but for n = 4 or 5 (quartic or quintic smoothing). The first row says 0 because m  
// is not allowed to be 2 this time. It starts at 3 instead.
```

```
double QuarQuin[11][26]={
```

```
{0},
```

```
{5,-30,75,131,75,-30,5,231},
```

```
{15,-55,30,135,179,135,30,-55,15,429},
```

```
{18,-45,-10,60,120,143,120,60,-10,-45,18,429},
```

```
{110,-198,-135,110,390,600,677,600,390,110,-135,-198,110,2431},
```

```
{2145,-2860,-2937,-165,3755,7500,10125,11053,10125,7500,3755,-165,-2937,-2860,2145,  
46189},
```

```
{195,-195,-260,-117,135,415,660,825,883,825,660,415,135,-117,-260,-195,195,4199},
```

```
{340,-255,-420,-290,18,405,790,1110,1320,1393,1320,1110,790,405,18,-290,-420,-255,340,  
7429},
```

```
{11628,-6460,-13005,-11220,-3940,6378,17655,28190,36660,42120,44003,42120,36660,28190,  
17655,6378,-3940,-11220,-13005,-6460,11628,260015},
```

```
{95,-38,-95,-95,-55,10,87,165,235,290,325,337,325,290,235,165,87,10,-55,-95,-95,-38,95,  
2185},
```

```
{1265,-345,-1122,-1255,-915,-255,590,1503,2385,3155,3750,4125,4253,4125,3750,3155,2385,  
1503,590,-255,-915,-1255,-1122,-345,1265,30015}
```

```

};

// Dynamically allocates memory for a row vector to contain a row of coefficients above.
double **coeff;
coeff = new double*[1];
coeff[0] = new double[25];

if(n==2 || n==3)
{
// Put the proper convoluting integers into "coeff".
for(i=0; i<2*m+1; i++)
coeff[0][i] = QuadCub[m-2][i];

// Use MatrixMult on coeff and Y, and put the result in B.
MatrixMult(coeff,Y,B,1,2*m+1,1);
// Divide B by the normalization factor.
B[0][0]=B[0][0]/QuadCub[m-2][i];
}

else if (n==4 || n==5)
{
for(i=0; i<2*m+1; i++)
coeff[0][i] = QuarQuin[m-2][i];
}

```

```

MatrixMult(coeff,Y,B,1,2*m+1,1);
B[0][0]=B[0][0]/QuarQuin[m-2][i];
}
delete[]coeff;
}

void CalcDeriv1(double **Y, double **B, int n, int m)
{
int i;
double Quad[11][26]={
{-2,-1,0,1,2,10},
{-3,-2,-1,0,1,2,3,28},
{-4,-3,-2,-1,0,1,2,3,4,60},
{-5,-4,-3,-2,-1,0,1,2,3,4,5,110},
{-6,-5,-4,-3,-2,-1,0,1,2,3,4,5,6,182},
{-7,-6,-5,-4,-3,-2,-1,0,1,2,3,4,5,6,7,280},
{-8,-7,-6,-5,-4,-3,-2,-1,0,1,2,3,4,5,6,7,8,408},
{-9,-8,-7,-6,-5,-4,-3,-2,-1,0,1,2,3,4,5,6,7,8,9,570},
{-10,-9,-8,-7,-6,-5,-4,-3,-2,-1,0,1,2,3,4,5,6,7,8,9,10,770},
{-11,-10,-9,-8,-7,-6,-5,-4,-3,-2,-1,0,1,2,3,4,5,6,7,8,9,10,11,1012},
{-12,-11,-10,-9,-8,-7,-6,-5,-4,-3,-2,-1,0,1,2,3,4,5,6,7,8,9,10,11,12,1300}
};

```

```

double CubQuar[11][26]={
{1,-8,0,8,-1,12},
{22,-67,-58,0,58,67,-22,252},
{86,-142,-193,-126,0,126,193,142,-86,1188},
{300,-294,-532,-503,-296,0,296,503,532,294,-300,5148},
{1133,-660,-1578,-1796,-1489,-832,0,832,1489,1796,1578,660,-1133,24024},
{12922,-4121,-14150,-18334,-17842,-13843,-7506,0,7506,13843,17842,18334,14150,4121,
-12922,334152},
{748,-98,-643,-930,-1002,-902,-673,-358,0,358,673,902,1002,930,643,98,-748,23256},
{6936,68,-4648,-7481,-8700,-8574,-7372,-5363,-2816,0,2816,5363,7372,8574,8700,7481,4648,
-68,-6936,255816},
{84075,10032,-43284,-78176,-96947,-101900,-95338,-79564,-56881,-29592,0,29592,56881,
79564,95338,101900,96947,78176,43284,-10032,-84075,3634092},
{3938,815,-1518,-3140,-4130,-4567,-4530,-4098,-3350,-2365,-1222,0,1222,2365,3350,4098,
4530,4567,4130,3140,1518,-815,-3938,197340},
{30866,8602,-8525,-20982,-29236,-33754,-35003,-33450,-29562,-23806,-16649,-8558,0,8558,
16649,23806,29562,33450,35003,33754,29236,20982,8525,-8602,-30866,1776060}
};

```

```

double QuinSex[11][26]={
{0},
{-1,9,-45,0,45,-9,1,60},

```

```

{-254,1381,-2269,-2879,0,2879,2269,-1381,254,8580},
{-573,2166,-1249,-3774,-3084,0,3084,3774,1249,-2166,573,17160},
{-9647,27093,-12,-33511,-45741,-31380,0,31380,45741,33511,12,-27093,9647,291720},
{-78351,169819,65229,-130506,-266401,-279975,-175125,0,175125,279975,266401,130506,
-65229,-169819,78351,2519400},
{-14404,24661,16679,-8671,-32306,-43973,-40483,-23945,0,23945,40483,43973,32306,8671,
-16679,-24661,14404,503880},
{-255102,349928,322378,9473,-348823,-604484,-686099,-583549,-332684,0,332684,583549,
686099,604484,348823,-9473,-322378,-349928,255102,9806280},
{-15033066,16649358,19052988,6402438,-10949942,-26040033,-34807914,-35613829,
-28754154,-15977364,0,15977364,28754154,35613829,34807914,26040033,10949942,
-6402438,-19052988,-16649358,15033066,637408200},
{-400653,359157,489687,265164,-106911,-478349,-752859,-878634,-840937,-654687,-357045,
0,357045,654687,840937,878634,752859,478349,106911,-265164,-489687,-359157,
400653,18747300},
{-8322182,6024183,9604353,6671883,544668,-6301491,-12139321,-15896511,-17062146,
-15593141,-11820675,-6356625,0,6356625,11820675,15593141,17062146,15896511,
12139321,6301491,-544668,-6671883,-9604353,-6024183,8322182,429214500}
};

```

```

double **coeff;
coeff = new double*[1];
coeff[0] = new double[25];

```

```

if(n==2)
{
for(i=0; i<2*m+1; i++)
coeff[0][i] = Quad[m-2][i];

MatrixMult(coeff,Y,B,1,2*m+1,1);
B[0][0]=B[0][0]/Quad[m-2][i];
}

```

```

else if (n==3 || n==4)
{
for(i=0; i<2*m+1; i++)
coeff[0][i] = CubQuar[m-2][i];

MatrixMult(coeff,Y,B,1,2*m+1,1);
B[0][0]=B[0][0]/CubQuar[m-2][i];
}

```

```

else if (n==5 || n==6)
{
for(i=0; i<2*m+1; i++)
coeff[0][i] = QuinSex[m-2][i];

```

```

MatrixMult(coeff,Y,B,1,2*m+1,1);
B[0][0]=B[0][0]/QuinSex[m-2][i];
}
delete[]coeff;
}

void CalcDeriv2(double **Y, double **B, int n, int m)
{
int i;
double QuadCub[11][26]={
{2,-1,-2,-1,2,7},
{5,0,-3,-4,-3,0,5,42},
{28,7,-8,-17,-20,-17,-8,7,28,462},
{15,6,-1,-6,-9,-10,-9,-6,-1,6,15,429},
{22,11,2,-5,-10,-13,-14,-13,-10,-5,2,11,22,1001},
{91,52,19,-8,-29,-44,-53,-56,-53,-44,-29,-8,19,52,91,6188},
{40,25,12,1,-8,-15,-20,-23,-24,-23,-20,-15,-8,1,12,25,40,3876},
{51,34,19,6,-5,-14,-21,-26,-29,-30,-29,-26,-21,-14,-5,6,19,34,51,6783},
{190,133,82,37,-2,-35,-62,-83,-98,-107,-110,-107,-98,-83,-62,-35,-2,37,82,133,190,33649},
{77,56,37,20,5,-8,-19,-28,-35,-40,-43,-44,-43,-40,-35,-28,-19,-8,5,20,37,56,77,17710},
{92,69,48,29,12,-3,-16,-27,-36,-43,-48,-51,-52,-51,-48,-43,-36,-27,-16,-3,12,29,48,69,92,26910}
};

```



```

double QuarQuin[11][26]={
{0},
{-13,67,-19,-70,-19,67,-13,132},
{-126,371,151,-211,-370,-211,151,371,-126,1716},
{-90,174,146,1,-136,-190,-136,1,146,174,-90,1716},
{-2211,2970,3504,1614,-971,-3016,-3780,-3016,-971,1614,3504,2970,-2211,58344},
{-31031,29601,44495,31856,6579,-19751,-38859,-45780,-38859,-19751,6579,31856,44495,
29601,-31031,1108536},
{-2132,1443,2691,2405,1256,-207,-1557,-2489,-2820,-2489,-1557,-207,1256,2405,2691,1443,
-2132,100776},
{-32028,15028,35148,36357,25610,8792,-9282,-24867,-35288,-38940,-35288,-24867,-9282,
8792,25610,36357,35148,15028,-32028,1961256},
{-12597,3876,11934,13804,11451,6578,626,-5226,-10061,-13224,-14322,-13224,-10061,-5226,
626,6578,11451,13804,11934,3876,-12597,980628},
{-115577,20615,93993,119510,110545,78903,34815,-13062,-57645,-93425,-116467,-124410,
-116467,-93425,-57645,-13062,34815,78903,110545,119510,93993,20615,-115577,
11248380},
{-143198,10373,99385,137803,138262,112067,69193,18285,-33342,-79703,-116143,-139337,
-147290,-139337,-116143,-79703,-33342,18285,69193,112067,138262,137803,99385,
10373,-143198,17168580}
};

```

```

double **coeff;

coeff = new double*[1];

coeff[0] = new double[25];

if(n==2 || n==3)
{
for(i=0; i<2*m+1; i++)
coeff[0][i] = QuadCub[m-2][i];

MatrixMult(coeff,Y,B,1,2*m+1,1);

B[0][0]=B[0][0]/QuadCub[m-2][i];
}

else if (n==4 || n==5)
{
for(i=0; i<2*m+1; i++)
coeff[0][i] = QuarQuin[m-2][i];

MatrixMult(coeff,Y,B,1,2*m+1,1);

B[0][0]=B[0][0]/QuarQuin[m-2][i];
}

delete[]coeff;
}

```

/* StringToInt takes a character string as input and returns an integer data type if possible. Main always reads the user's response as a string to prevent the program from crashing, but if the program needs to know what number the user entered into the string, then this script is necessary to convert it. It returns -1 if it fails. */

```
int StringToInt(char string[SL])
```

```
{
```

```
int i = 0, j = 0, number = 0, digit = 0;
```

```
bool ok = 1, end = 0;
```

```
// If the first character is null, then don't look any further, just quit.
```

```
if(string[0] == '\0')
```

```
ok = 0;
```

```
// Figure out how many digits (j) there are before the null. If anything other than a digit is
```

```
// encountered, quit with error. Also, the integer being read can't be larger than 999,999,999.
```

```
while (ok && !end && i < SL && i <= 9)
```

```
{
```

```
if(string[i] == '0' || string[i] == '1' || string[i] == '2' || string[i] == '3' || string[i] == '4' || string[i] == '5' ||
```

```
string[i] == '6' || string[i] == '7' || string[i] == '8' || string[i] == '9')
```

```
i++;
```

```
else if(string[i] == '\0')
```

```
{  
end = 1;  
j = i-1;  
}
```

```
else  
ok = 0;  
}
```

// If a valid integer is present, this converts it by associating each digit with its corresponding

// power of 10 and adding together. For example: $1,234 = 1000 + 200 + 30 + 4$.

```
if(ok && end)
```

```
{
```

```
i=0;
```

```
while(j >= 0)
```

```
{
```

```
if(string[i] == '0')
```

```
digit = 0;
```

```
else if(string[i] == '1')
```

```
digit = 1;
```

```
else if(string[i] == '2')
```

```
digit = 2;
```

```
else if(string[i] == '3')
digit = 3;
else if(string[i] == '4')
digit = 4;
else if(string[i] == '5')
digit = 5;
else if(string[i] == '6')
digit = 6;
else if(string[i] == '7')
digit = 7;
else if(string[i] == '8')
digit = 8;
else if(string[i] == '9')
digit = 9;

number = number + digit * pow(10.0,j);

i++;
j--;
}
}

else
number = -1;
```

```
return number;
```

```
}
```

```
void main()
```

```
{
```

```
int i, n, m, skip, order = -1;
```

```
bool outfileok, infileok, skipok, nok, mok, check;
```

```
char inname[SL], outname[SL], answer[SL];
```

```
ofstream outfile;
```

```
ifstream infile, testfile;
```

```
// This warning is for simplicity, but the user can specify a different file path.
```

```
cout << "Please make sure the file you wish to use" << endl << "is in the same directory as this  
program." << endl;
```

```
// This loop determines whether the user wants to smooth or differentiate data, and if the latter,
```

```
// then first or second derivative. Sets "order" accordingly.
```

```
while(order == -1)
```

```
{
```

```
cout << "\nDo you want to smooth or differentiate data? (S/D): ";
```

```
cin.getline(answer,SL);
```

```

if((answer[0]=='s' || answer[0]=='S') && answer[1]=='\0')
order = 0;

else if ((answer[0]=='d' || answer[0]=='D') && answer[1]=='\0')
{
while(order == -1)
{
cout << "\nWhat order derivative do you want to perform? (1 or 2): ";
cin.getline(answer,SL);

if(answer[0]=='1' && answer[1]=='\0')
order = 1;

else if(answer[0]=='2' && answer[1]=='\0')
order = 2;

else
cout << "\nInvalid choice.\n";
}
}

else
cout << "\nInvalid choice.\n";

```

```

}

infileok = 0;

// Ask the user for the input file name.

while(!infileok)

{

if(order==0)

{

cout << "\nWhat is the name of the file you wish to smooth?" << endl << "For example,

        \nToSmooth.dat\ ": ";

}

else

{

cout << "\nWhat is the name of the file you wish to differentiate?" << endl << "For example,

        \nToDiff.dat\ ": ";

}

cin.getline(inname,SL);

// Try to open the input file. If it fails, tell the user and ask for a new name. If it works, then close

// the file and move on.

testfile.open(inname);

```



```

if(testfile.fail())
{
testfile.close();
testfile.clear();
cout << "\nFailed to open \"" << inname << "\"\n";
infileok = 0;
}

else
{
testfile.close();
testfile.clear();
infileok = 1;
}
}

skipok = 0;

// Ask the user how many lines are in the input file's header so that they can be skipped later.
while(!skipok)
{
cout << "\nHow many lines in \"" << inname << "\" need to be skipped?: ";
cin.getline(answer,SL);
skip = StringToInt(answer);
}

```

```

if(skip != -1)
skipok = 1;

if(!skipok)
cout << "\nInvalid number.\n";
}

nok = 0;

// Ask the user what order of polynomials to fit the data with. A lower n smoothes over more
// features than a higher n (for both smoothing and derivatives).
while(!nok)
{
cout << "\nThe program will fit polynomials of order n to the data.\n";

if(order == 1)
cout << "What is n? (2-6): ";

else
cout << "What is n? (2-5): ";

cin.getline(answer,SL);
n = StringToInt(answer);

```

```

if(n==2 || n==3 || n==4 || n==5 || (n==6 && order==1))
nok = 1;

else
cout << "\nInvalid number.\n";
}

mok = 0;

// Ask the user how many data points to fit at once. A higher m smoothes over more features than
// a lower m. A higher m will also crop more data at the beginning and end.
while(!mok)
{
cout << "\nThe program will use 2m+1 data points for each fit.\n";

if(n <= 3 || (n==4 && order==1))
cout << "What is m? (2-12): ";

else
cout << "What is m? (3-12): ";

cin.getline(answer,SL);
m = StringToInt(answer);

```

```

if(m==12 || m==11 || m==10 || m==9 || m==8 || m==7 || m==6 || m==5 || m==4 || m==3 || (m==2
    && (n<=3 || (n==4 && order==1))))
    mok = 1;

else

cout << "\nInvalid number.\n";

}

outfileok = 0;

// Ask the user for the output file name.

while(!outfileok)

{

if(order==0)

{

cout << "\nWhat do you want to name the smoothed file?"

<< "\nFor example, \"Smoothed.dat\": ";

}

else

{

cout << "\nWhat do you want to name the differentiated file?"

<< "\nFor example, \"Derivative.dat\": ";

}

}

```

```

}

cin.getline(outname,SL);

// Try to open the output file. If it fails, then it does not already exist, so we can create it without
// a problem. If it succeeds, then there are two possibilities below.

testfile.open(outname);

if(testfile.fail())
{
if(outname[0] != '\0')
outfileok = 1;

testfile.close();
testfile.clear();
}

else
{
testfile.close();
testfile.clear();

// Check whether the input and output file names are the same. This is not allowed.
if(strcmp(inname,outname)==0)

```

```

{
cout << "\nOutput file cannot be same as input file.\n";
outfileok = 0;
}

else
{
check = 1;

// If the output file already existed and was not the same as the input file, then ask the user
// whether they want to replace that file. If not, then ask for a new file name.

while(check)
{
cout << "\n\"" << outname << "\" already exists. Replace it? (Y/N): ";
cin.getline(answer,SL);

if((answer[0]=='y' || answer[0]=='Y') && answer[1]=='\0')
{
outfileok = 1;
check = 0;
}

else if((answer[0]=='n' || answer[0]=='N') && answer[1]=='\0')
{

```

```
outfileok = 0;
```

```
check = 0;
```

```
}
```

```
else
```

```
{
```

```
outfileok = 0;
```

```
cout << "\nInvalid choice.\n";
```

```
}
```

```
}
```

```
}
```

```
}
```

```
}
```

```
// Open the input file and create the output file.
```

```
infile.open(inname);
```

```
outfile.open(outname);
```

```
// Throw away the first few header lines if the user said to.
```

```
for(i=0;i<skip;i++)
```

```
infile.getline(answer,SL);
```

```
int R=2*m+1;
```

```

// Allocate memory for B, X, and Y. X and Y will hold 2*m+1 numbers at once. B will only
// have one.

double **B;

B = new double*[1];

B[0] = new double[1];

double **Y;

Y = new double*[R];

for(i=0;i<R;i++)

Y[i] = new double[1];

double **X;

X = new double*[R];

for(i=0;i<R;i++)

X[i] = new double[1];

// Get the first 2*m+1 X and Y data points from the input file.

for(i=0;i<2*m+1;i++)

{

infile >> X[i][0] >> Y[i][0];

infile.get();

}

```



```

// Calculate the step size from one x-value to the next. (Should all be the same.)
double diff = abs(X[1][0]-X[0][0]);

// Send Y, B, n, and m to the appropriate fitting/derivative function until end of file.
while(!infile.eof())
{
if(order == 0)
{
CalcFit(Y, B, n, m);

// Make a row in the output file: the current x-value, then tab, then the current new y-value.
outfile << X[m][0] << "\t" << B[0][0] << endl;
}

else if(order == 1)
{
CalcDeriv1(Y, B, n, m);

outfile << X[m][0] << "\t" << (B[0][0])/diff << endl;
}

else
{
CalcDeriv2(Y, B, n, m);

outfile << X[m][0] << "\t" << (B[0][0])/(diff*diff) << endl;
}
}

```

```

}

// Advance X and Y one row in the input file. Note that this only requires reading in one line
// from the file since 2*m of the rows you need are already in X and Y. Just shift them one spot.
for(i=0;i<2*m;i++)
{
X[i][0]=X[i+1][0];
Y[i][0]=Y[i+1][0];
}
infile >> X[i][0] >> Y[i][0];
infile.get();
}

// Close the files and clean up the memory.
infile.close();
outfile.close();
delete[]B;
delete[]Y;
delete[]X;

cout << "\nDone!\n\nPress \"Enter\" to terminate...";
cin.get();
}

```

Appendix H: Periodogram Code

```
function [ f,S ] = periodogram( x,max )
```

```
% This is a MATLAB function to compute the power spectral density of a signal recorded as a  
% function of time.
```

```
%
```

```
% Inputs:
```

```
% x - A vector, the signal measurements in chronological order. They must be separated by
```

```
% equal-length steps in time (duration set in the code).
```

```
% max - A scalar, the maximum frequency you want to calculate out to, in Hz. The minimum
```

```
% frequency is zero by default.
```

```
%
```

```
% Outputs:
```

```
% f - A vector, all the frequencies at which the periodogram was computed, in Hz.
```

```
% S - A vector, the power spectral density of the signal at each frequency, in units of the signal's
```

```
% measurement unit squared.
```

```
% Set the time step interval in seconds by changing t. It is currently 1 because the graphene
```

```
% height-time data had one point per second.
```

```
t = 1;
```

```
% The program here automatically determines how many data points are in your signal.
```

```
N = length(x);
```

```
T = N*t;
```

```
% This sets the frequency space to be considered. 0 Hz is the minimum, max is the maximum,  
% and there will be 1000 steps between them unless you change it here.
```

```
f = linspace(0,max,1000);
```

```
f = transpose(f);
```

```
a = t^2/T;
```

```
% Initialize the S vector to store final results.
```

```
S = zeros(1000,1);
```

```
% This double loop calculates S at each f using the periodogram definition at the end of
```

```
% Appendix F. If you change the length of f above, then also change the upper limit on c here.
```

```
for c = 1:1000
```

```
B = 0;
```

```
for n = 1:N
```

```
B = B + x(n)*exp(-1i*2*pi*f(c)*n);
```

```
end
```

```
S(c) = a*(B*conj(B));
```

```
end
```

```
end
```